Chapter 2
Infrared Spectroscopy of Chromophore-Labeled Water Clusters Phenol-$(H_2O)_n$ (n < ~50)

Abstract To analyze hydrogen bond network structures consisting of tens of water molecules, we measured moderately size-selective IR spectra of large, labeled water clusters phenol-$(H_2O)_n$ in the OH stretch region. The observed spectral features were analyzed in terms of hydrogen bond ring size motifs and coordination numbers of water molecules. The detailed analyses of the free OH band indicated that the observed low-frequency shift originates from the cooperativity of hydrogen bonds and the structural development from the highly strained 4-membered ring motif to the more relaxed 5- and 6-membered ring motifs. The suppression of free OH band intensity with an increase of n represents the increase of the abundance of 4-coordinated waters. We expect that the present characterization method of hydrogen bond networks may be applicable to more complicated, condensed phase water.

Keywords Phenol-water clusters · Supersonic jet expansion · IR–UV spectroscopy · Hydrogen bond network distortion · Coordination number analyses of water

2.1 Introduction

As described in Chap. 1, size-selective IR spectroscopy of large water clusters consisting of ten or more molecules is necessary to study large-scale, bulky hydrogen-bonded water networks. The clear structural differences can be seen between small clusters ($n < \sim 10$) and bulk water. The most obvious differences are coordination numbers of molecules and ring size of hydrogen bond networks; small clusters mainly consist of 3-coordinated molecules and 4-membered rings, while ice Ih consists of 4-coordinated molecules and 6-membered rings (see Fig. 1.5). The main purpose of this chapter is to bridge the gap by extending spectroscopic method to larger water clusters $(H_2O)_n$ ($n > \sim 10$).

K. Mizuse, *Spectroscopic Investigations of Hydrogen Bond Network Structures in Water Clusters*, Springer Theses, DOI: 10.1007/978-4-431-54312-1_2,

Previously, several approaches have been made towards size-selective spectroscopy of large water clusters as introduced in Sect. 1.3.3. Figure 2.1 shows IR spectra reported in these studies [1–6]. Unfortunately, these studies lack size-selectivity and/or size variety. As a result, the structures of large clusters have not necessarily been discussed on the basis of experimental spectra.

On the other hand, there is essentially no difficulty in the size-selection in theoretical calculations, although exponential increase of possible isomer structures is another serious problem for large-sized clusters. Recent development of theories, algorithms, and computer resources make it possible to treat relatively large water networks with reasonable accuracy. Extensive theoretical studies on the $(H_2O)_n$ ($n < \sim 50$) clusters, from empirical methods to sophisticated density functional theory and high-level *ab initio* combined with minimum search algorisms, have predicted that the 4-membered ring motif will become less important with increasing cluster size while the 5- and 6-membered ring motifs will become superior [5, 7–22]. For example, Kazimirski and Buch [7] have carried out a low energy isomer search for $(H_2O)_{48}$ with the empirical TIP4P potential. In the reported structure of $(H_2O)_{48}$ (Fig. 2.2), only 18 % of rings are 4-membered and 5- and 6-membered rings become superior, although $(H_2O)_8$ consists only of 4-membered rings. Another structural transition, the appearance and increase of 4-coordinated water molecules and also the interior formation have been also suggested in this size region [5, 7–22]. For example, Lagutschenkov et al. [10] have suggested the "interior" water molecules arise at around $n = 17$ on the basis of their empirical and high-level *ab initio* calculations (Fig. 2.2). On the other hand, smaller clusters are categorized as "all surface" types, in which all the water molecules are located at the surface of the network. If molecules are completely inside a network, they should be

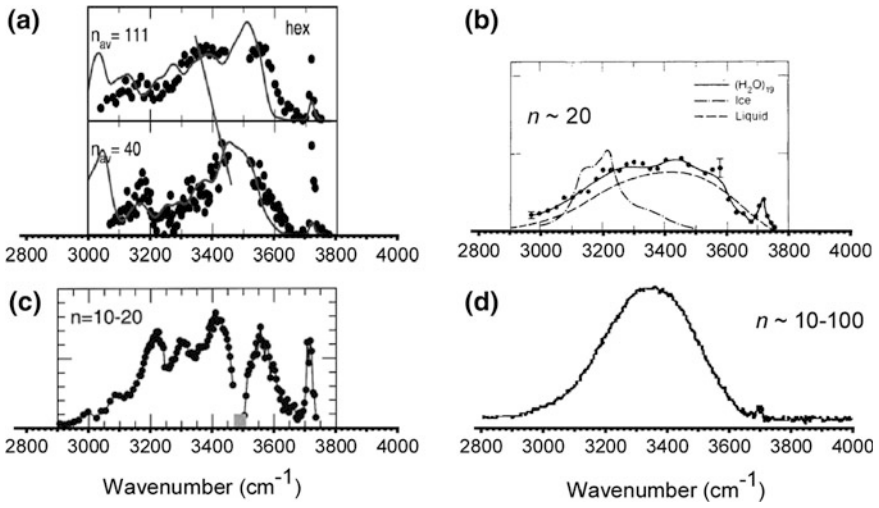

Fig. 2.1 Previously reported IR spectra of roughly size-selected or size-estimated large water clusters. **a** From Ref. [4], **b** from Ref. [2], **c** from Ref. [1], and **d** from Ref. [3]

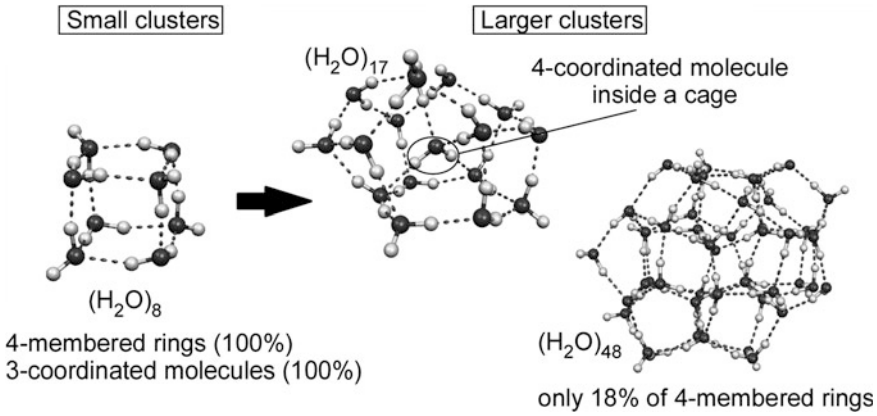

Fig. 2.2 Theoretically predicted cluster structures and structural developments of $(H_2O)_n$ ($n > \sim 10$). Appearance of 4-coordinated molecules and decrease of 4-membered rings is displayed

4-coordinated. This implies that the signature of 4-coordinated molecules would be observed in the size range ($n \sim$ a few tens). To study high order structures of hydrogen-bonded water networks, observation of such interior molecules should be an important step. Figure 2.2 indicates some characteristic cluster structures of $(H_2O)_n$ highlighting the predicted structural changes in the $n > 10$ region. As mentioned here, recent developments in computational chemistry have stimulated size-selective spectroscopy of water clusters consisting tens of molecules. However, correlations between detailed cluster structures and IR spectral features have not been extensively examined. This fact also indicates the importance of size-selective IR spectra of large water clusters.

An experimental bottleneck relates to the detection technique. Clusters of interest are formed by the supersonic jet expansion technique [23], which is the most popular method for cluster production. In this method, a gaseous mixture of sample molecules is expanded into a vacuum chamber. Only low concentration is achieved in the molecular/cluster beam and as a result, direct photo absorption detection, which detects decrease of light intensity, is generally impossible. We therefore have to utilize highly sensitive detection techniques, the fluorescence or ionization detection of gas phase molecular and cluster samples. Water clusters are, of course, not fluorescent. For spectroscopic purposes, ionization by photons is preferable [24], however the ionization energy of water molecules (12.62 eV) is very high and we need a short wavelength vacuum-ultraviolet light ($< \sim 100$ nm, depending on the cluster size [25–27]) or a very intense light source such as a femtosecond laser for photoionization of water clusters [28, 29]. Unfortunately, both of these were not available for our procedures. This problem has made it difficult to select the cluster size with photoionization mass spectrometry and to measure IR spectra with photoionization-based spectroscopic technique, as shown below.

To overcome these problems, we introduced a label to the water clusters. Phenol as an ultraviolet (UV) chromophore was used as a spectroscopic label (Fig. 2.3). The chromophore-labeled water clusters have the advantage of possessing an UV chromophore (the phenyl ring), which enables us to apply various spectroscopic techniques such as resonant two-photon ionization (R2PI) based on UV electronic transition. Since the earlier stages of spectroscopic studies on gas-phase hydrated clusters, phenol-$(H_2O)_n$ have been studied extensively by, for example, fluorescence excitation, R2PI, and various double resonance spectroscopies [30–50].

As shown in Sect. 1.3, IR spectroscopy is a powerful tool to probe hydrogen bond networks. IR–UV double resonance spectroscopy is a technique to measure a size- and isomer-specific IR spectra of gas phase molecules and clusters with a chromophore [44, 51, 52]. This technique was developed by Lee's group in the 1980s [51]. It has been applied to many molecules/clusters including phenol-$(H_2O)_n$ and was successful in characterizing structures and many other properties [44, 52]. Here, an overview of this method is given. The energy scheme is shown in Fig. 2.4. First, UV light is tuned to the wavelength of vibronic transition of the species of interest. Resonant multiphoton ionization signals or fluorescent signals from the electronic excited state are monitored as a measure of population of the ground vibrational state. While monitoring this signal, the IR light pulse is irradiated prior to the UV light pulse. When IR light is absorbed, vibrational transition occurs and the ground vibrational level population is decreased, leading a depletion of the monitored signal. A depletion signal as a function of IR wavelength can be regarded as an IR spectrum. In this method, if the UV wavelength is tuned to size- and isomer-specific transition, the measured IR spectrum is size- and isomer-selective.

Previous studies, especially those on vibrational spectroscopy (IR–UV double resonance spectroscopy) in the OH stretch region, showed that phenol-$(H_2O)_n$ are structural analogues of neat $(H_2O)_{n+1}$ because the hydroxy group of the phenol plays a compatible role to that of a water in the hydrogen bond network [43, 49, 50] (Fig. 2.5). Of course, because phenol is a weak acid molecule, it may act as a stronger hydrogen bond donor, and the hydrogen bond network of phenol-$(H_2O)_n$ is more or less perturbed from the neat $(H_2O)_n$. The reported results, that both labeled and neat clusters have essentially the same network, indicate that perturbation from UV-chromophore is too small to affect hydrogen-bonded water networks in these systems. For phenol-$(H_2O)_n$ [42, 43, 49] and a similar system, benzene-$(H_2O)_{n+1}$ [52–57], size-selected IR spectra have been measured up to $n \leq 8$ using their size-

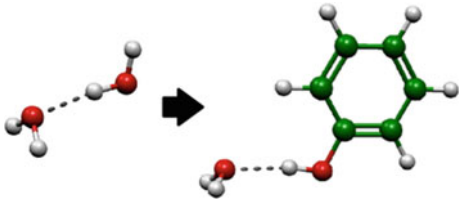

Fig. 2.3 Introduction of UV-chromophore (label) to water clusters

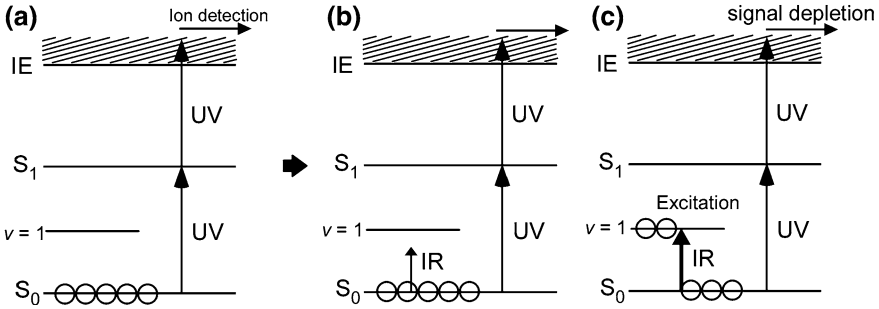

Fig. 2.4 Energy scheme in IR–UV double resonance spectroscopy. *Open circles* denote a molecule/cluster in various states. **a** First, ground vibrational state population was probed with R2PI. **b**, **c** IR light is irradiated and its wavelength is scanned. **c** When IR light is absorbed, vibrational excitation results in the ion signal depletion

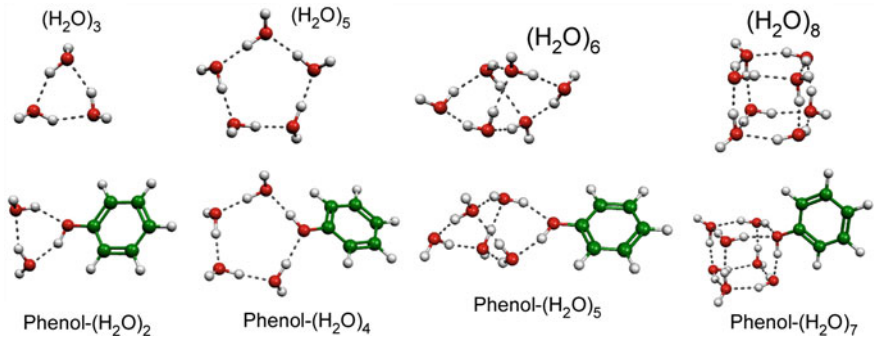

Fig. 2.5 Experimentally characterized structures of phenol-$(H_2O)_n$ and $(H_2O)_{n+1}$. Both hydrogen bond network structures are essentially the same

specific UV transitions. These IR spectroscopic studies on chromophore-labeled water clusters have pioneered structural studies on small-sized water networks, as those of neat $(H_2O)_n$ clusters [2, 58–63] have done.

Here, we comment on the choice of the label. There have been other labels used for water clusters. Benzene-$(H_2O)_n$ and Na-$(H_2O)_n$ clusters have been also studied with photoionization-based methods [52–57, 64–68]. In the case of benzene-$(H_2O)_n$, hydrogen-bonded networks are pure water networks, while phenol-$(H_2O)_n$ contains a phenol molecule in a network. Despite this advantage of benzene, in such a cluster, a benzene ring is bound to an OH moiety of H_2O via an OH…π interaction [53, 54, 69]. Such an interaction is absent from pure water networks and therefore, spectral interpretation would become complicated [53, 69]. Furthermore, an OH…π interaction is generally weaker than hydrogen bonding, therefore yields of benzene-$(H_2O)_n$ are smaller than those of phenol-$(H_2O)_n$. For Na-$(H_2O)_n$, single UV photon ionization can be applied, however, interaction

between a water network and an unpaired electron on Na seems ignorable [67, 68]. According to these considerations, we employed a phenol molecule as a label.

For larger-sized clusters ($n > \sim 10$) with a chromophore, UV absorption bands are generally broadened and IR–UV double resonance spectroscopy has been considered useless for size selection. In this study, however, we use the scheme of the IR–UV double resonance but utilize only photoionization mass spectrometry to select the cluster size. Though we sacrifice rigorous size-selection because of fragmentation upon ionization, we still achieve moderate size-selectivity in the IR spectral measurement of phenol-$(H_2O)_n$ by monitoring the [phenol-$(H_2O)_n$]$^+$ ion signal. In this study, we measured IR spectra of roughly size-estimated clusters to probe hydrogen bond networks of 10 or more water molecules.

2.2 Experimental

2.2.1 Overview of Infrared Spectroscopy

Here, a brief overview of experimental methods is given and details are shown in the following sections. The gas phase phenol-$(H_2O)_n$ clusters were produced in a pulsed supersonic jet expansion of the gaseous phenol/water mixture diluted with helium. IR spectra of moderately size-selected phenol-$(H_2O)_n$ (n = 11–49) in the free OH stretch region (2,800–3,800 cm^{-1}) were measured by the IR–UV double resonance technique combined with mass spectrometry. Figure 2.6 shows an energetic scheme of the present "modified" IR–UV double resonance spectroscopy. The [phenol-$(H_2O)_n$]$^+$ ions produced by one-color resonant two-photon ionization (R2PI) of neutral clusters were mass-selected by a time-of-flight (TOF) mass spectrometer. Due to fragmentation upon ionization, [phenol-$(H_2O)_n$]$^+$ ions can be produced by R2PI of phenol-$(H_2O)_{n+\Delta n}$ (Δn is the number of evaporated water molecules upon ionization). As we will discuss later, the maximum Δn upon one-color R2PI is estimated to be 6 or less with the aid of a conservation law of energy (for details, see Sect. 2.2.3.2). The [phenol-$(H_2O)_n$]$^+$ ion intensity can be a measure of the ground state population of phenol-$(H_2O)_{n+\Delta n}$ ($0 \leq \Delta n \leq 6$). Then an IR pulse was introduced prior to the UV pulse and its frequency was scanned. When an IR transition occurs in phenol-$(H_2O)_{n+\Delta n}$, the monitored [phenol-$(H_2O)_n$]$^+$ signal decreases because of the vibrational predissociation of the clusters. IR spectra were thus measured by monitoring the ion intensity while scanning IR wavelength. In typical IR–UV double resonance spectroscopy, just a vibrational population transfer (excitation) is required to observe the dip signal [51], however, when a broadened UV transition is used, species in a vibrational excited state might also absorb UV light and then, vibrational dissociation would be needed for depletion spectroscopy. Of course, if the UV transition probability between the vibrational ground and excited states is different, IR-induced signal arises. However, the exact evaluation of such transition probability is beyond the scope of this work.

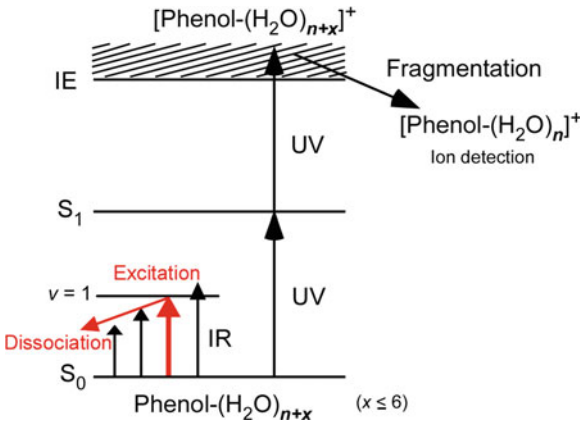

Fig. 2.6 Energy scheme in "modified" IR–UV double resonance spectroscopy used in the present study

2.2.2 Setup

2.2.2.1 Vacuum Chamber

Figure 2.7 shows the scheme of the vacuum chamber used in this study. This chamber consists of a supersonic jet expansion cluster source and a time-of-flight (TOF) mass spectrometer. This chamber was evacuated by two turbomolecular pumps, backed by rotary pumps.

In the cluster source region, the gaseous mixture of phenol (trace), water (trace), and helium (0.3 MPa) was expanded into a chamber through a pulsed valve (General valve Series 9, 0.5 mm nozzle diameter, Parker). The gas pulse was skimmed by a skimmer (2 mm hole diameter) and introduced to the interaction region, between the repeller and extractor electrodes of time-of-flight mass spectrometer.

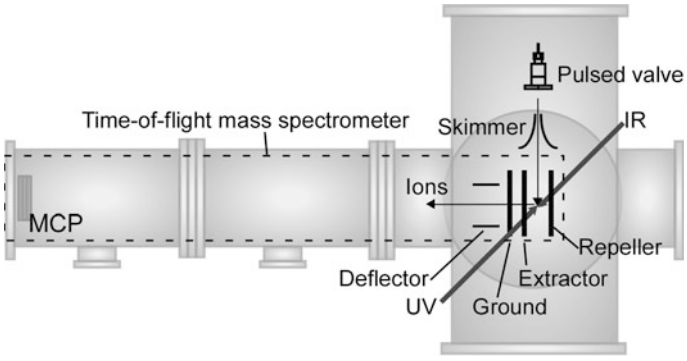

Fig. 2.7 Scheme of the vacuum chamber used in the present study

The time-of-flight mass spectrometer moiety was equipped with a 2-step acceleration region to improve mass resolution (Wiley-McLaren type [70]). The deflector was also equipped to compensate for the initial velocity, which is perpendicular to the TOF axis. Clusters are ionized by UV pulse between the repeller (typically +2500 V) and extractor (∼+1500 V) electrodes. Ions were extracted toward TOF tube (grounded), in which ions were mass-separated and then detected with a stack of microchannel plates (MCP).

2.2.2.2 Laser Systems

Figure 2.8 shows a diagram of the experimental setup. UV light was the second harmonic (SHG) of a dye laser output (Laser Analytical System LDL20505 with Coumarin 540A dye) pumped by a third harmonics (355 nm) of a Nd:YAG laser (1064 nm, Surelite III, Continuum). UV light was introduced to the middle of the repeller and extractor electrodes of time-of-flight mass spectrometer. A plano-convex quartz lens ($f = 500$ mm) was used for focusing the UV light. IR light was obtained by the difference frequency generation (DFG) with a $LiNbO_3$ crystal between the second harmonic (532 nm) of a Nd:YAG laser (1064 nm, Surelite III, Continuum) and an output of a dye laser (ND6000, Continuum, with DCM and LDS698 dyes). The optical path of the IR light was aligned to the same axis as the UV light from the opposite side. The IR light was focused by a plano-convex CaF_2 lens ($f = 250$ mm). In both systems, autotrackers (Inrad) were used to keep the phase matching angle while scanning wavelength. IR power was monitored by installing a CaF_2 beam sampler plate and an IR power meter (Molectron). The wavelength of the IR light was calibrated (in vacuum wavenumbers) by recording an ambient water vapor spectrum. Figure 2.9 shows a typical power curve of IR light obtained with DFG. The gap of around 3,500 cm^{-1} is due to the IR absorption by water impurities in the $LiNbO_3$ crystal. The wavelength of the UV light was calibrated in vacuum wavenumbers by recording a reported R2PI spectrum of phenol-$(H_2O)_{0–2}$.

2.2.2.3 Measurement System

Two YAG lasers and a pulsed valve were triggered by TTL outputs (10 Hz) from digital delay generators (DG 535, SRS). Ion signals from MCP were amplified (wide band preamplifier BX-31A, NF Electronic Instruments) and transferred to an oscilloscope (TDS 640A, 500 MHz, Tektronix) and a boxcar integrator (SR250, SRS). Both of which were triggered by a photodiode, which monitored emissions from Surelite. The oscilloscope was used for monitoring ion signals, gate signals of the boxcars, and IR power. It was also used for the measurement of TOF mass spectra.

For IR measurements, the ion signal of interest and IR power signal were averaged with SR250, and their data were sent to a digitizer (analog-to-digital converter) (SR245, SRS). Thus obtained data points were transferred to a computer

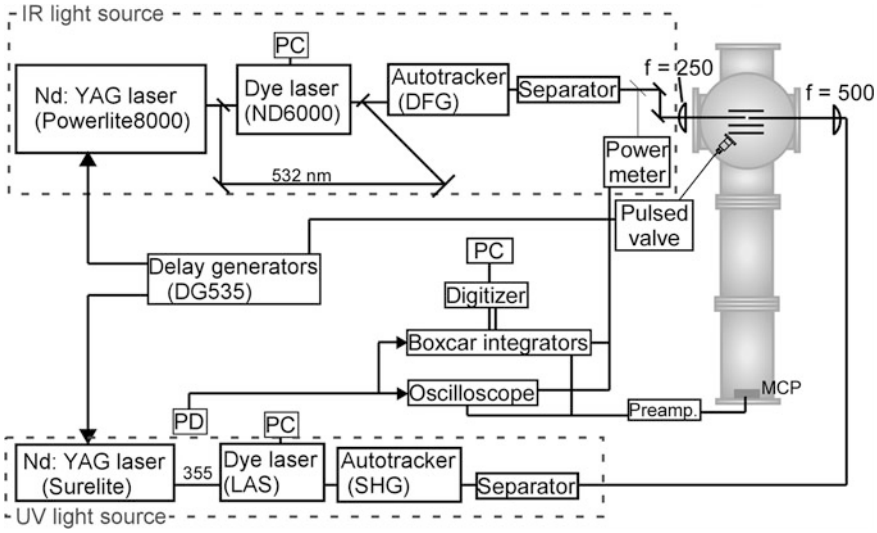

Fig. 2.8 Schematic diagram of the experimental setup

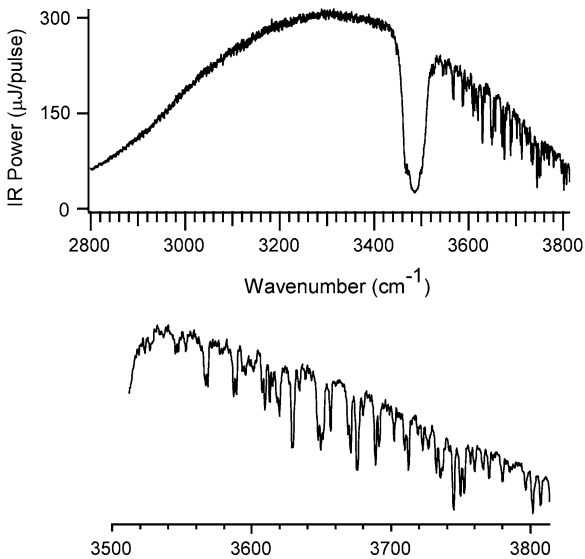

Fig. 2.9 Typical power curve of IR light source obtained with DFG

and plotted as a function of IR wavelength. Here, IR wavelength was scanned by operating a ND6000 with a constant speed scan mode. The observed raw IR spectra were normalized by IR power.

In the long-range scan (e.g. for the whole OH stretch region 2,800–3,800 cm^{-1}), the signal intensity sometimes changed in time due to the valve conditions and for other reasons. To improve the quality of observed spectra, the active baseline subtraction technique was applied to reduce artifacts by fluctuation

of the signal baseline. For this technique, the pulsed valve and the pulsed UV light were operated at 10 Hz while the pulsed IR light was at 5 Hz. The (raw) IR spectral data points were obtained from the differences in the ion intensity with and without the IR irradiation.

2.2.3 Measurements

2.2.3.1 Resonant 2-Photon Ionization of Phenol-$(H_2O)_n$

Figure 2.10 shows the one-color R2PI spectra obtained by monitoring [phenol-$(H_2O)_n$]$^+$ while scanning the UV wavelength. The spectra of the phenol$^+$ and phenol-$(H_2O)_1^+$ channels show essentially the same features as those reported previously [32, 35, 40, 43, 44]. In Fig. 2.10, only a structureless absorption band is seen for $n \geq 9$. The maximum size of the cluster, which shows sharp vibronic bands, has been reported to be $n = 12$ (by two-color R2PI spectroscopy, which minimizes the fragmentation) [48]. Contribution of larger clusters due to fragmentation and inherent broadening in large-sized clusters would wash out sharp spectral features in the present spectra. The UV frequency was tuned to 36,254 cm^{-1}, which is at near the maximum of the broad absorption of large-sized

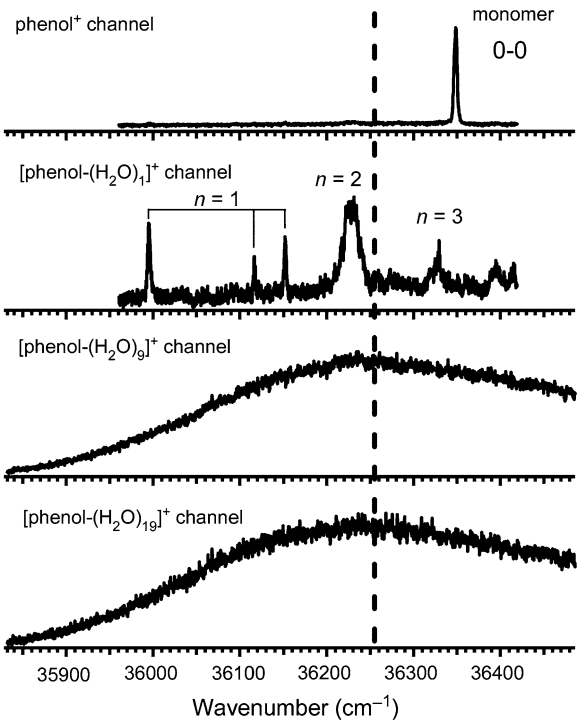

Fig. 2.10 One-color resonant two-photon ionization spectra of phenol-$(H_2O)_n$ obtained by monitoring [phenol-$(H_2O)_n$]$^+$ ions. Assignments were taken from previous studies. The *dashed line* indicates the UV photon energy, 36,254 cm^{-1}, used for the photoionization in the IR spectral measurements

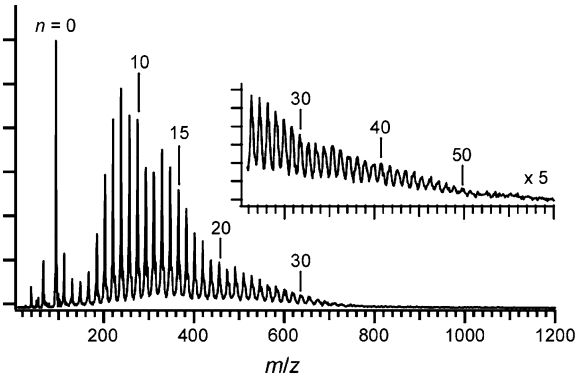

Fig. 2.11 Time-of-flight mass spectrum of [phenol-$(H_2O)_n$]$^+$ obtained with 36,254 cm^{-1} resonant 2-photon ionization

clusters, and the [phenol-$(H_2O)_n$]$^+$ ion intensity was monitored. Figure 2.11 shows a R2PI mass spectrum recorded by irradiating the 36,254 cm^{-1} UV light. Efficient cluster detection of up to $n < \sim 50$ was achieved.

We note that an application of two-color R2PI spectroscopy with an ionization UV pulse at a suitable frequency should reduce the excess energy and suppress fragmentation upon ionization [48]. Though we actually applied the two-color R2PI scheme for the present large-sized clusters, the two-color ionization signal was hardly detectable. This is because the production yields of the large-sized clusters are so low that we needed to use a relatively intense UV pulse for the first electronic excitation, and it significantly reduced the ionization by the second UV pulse.

2.2.3.2 Evaluation of Size-Selectivity

Because hydrogen-bonded clusters usually suffer from fragmentations in an ionization process, it is difficult to precisely measure the size distribution of the neutral clusters only from mass spectrometry. However, for phenol-$(H_2O)_n$, the number of evaporated water molecules (Δn) upon one-color R2PI can be estimated to be 6 or less by the energetics calculations. Figure 2.12 shows the schematic energy diagram on the photoionization and dissociation of phenol-$(H_2O)_n$. Because the one water loss channel ([M-$(H_2O)_n$]$^+$ → [M-$(H_2O)_{n-1}$]$^+$ + H_2O) is the major dissociation path in cationic hydrated clusters with excess energies [71], we assume the sequential evaporation of water molecules one by one upon ionization. Then, the maximum Δn is evaluated by

$$\text{maximum } \Delta n = E_{\text{excess}}/D(\text{D}_0) \tag{2.1}$$

where E_{excess} is the maximum excess energy upon ionization and $D(\text{D}_0)$ is the dissociation energy of the one water-loss channel in the cationic state. Because [phenol-$(H_2O)_n$]$^+$ ($n \geq 3$ or 4) forms an intracluster proton-transferred [PhO·-H$^+$$(H_2O)_n$] type structure [72–74], the dissociation energies of H$^+$$(H_2O)_n$, which have been measured by the mass spectrometric technique [75], can be used as $D(\text{D}_0)$ here. E_{excess} is given by:

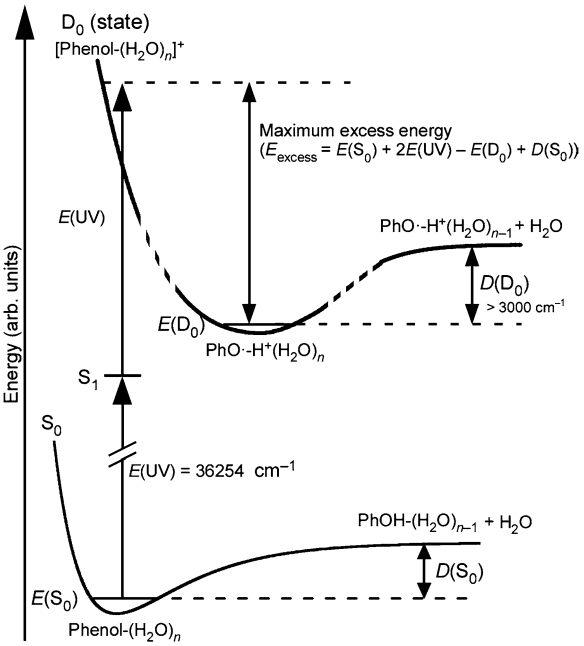

Fig. 2.12 Schematic energy diagram on the photoionization and dissociation of phenol-$(H_2O)_n$

$$E_{\text{excess}} = 2E(\text{UV}) - [E(\text{D}_0) - E(\text{S}_0)] + D(\text{S}_0) \tag{2.2}$$

where $E(S_0)$ and $E(D_0)$ are the absolute energies of phenol-$(H_2O)_n$ and $[PhO\cdot\text{-}H^+(H_2O)_n]$ at the zero-point level, respectively, then $[E(D_0) - E(S_0)]$ is the adiabatic ionization energy of the phenol-$(H_2O)_n$; $E(UV)$ is the UV photon energy (36,254 cm^{-1}), and $D(S_0)$ is the dissociation energy in the S_0 state. In Eq. (2.2), $D(S_0)$ accounts for the maximum internal energy of the phenol-$(H_2O)_n$. Though we employ the supersonic jet cooling technique, the clusters have finite internal energies (temperatures). In addition, broadened electronic spectra of the large-sized clusters prevent us from evaluating the internal energy. The maximum internal energy of the cluster should be lower than $D(S_0)$, because clusters with internal energy higher than $D(S_0)$ spontaneously dissociate into smaller-sized clusters prior to arrival at the interaction region with the lasers.

Considering these relationships, we examined the energetics of dissociation of phenol-$(H_2O)_{11,19}$ following the photoionization, as typical examples. $E(S_0)$ and $E(D_0)$ were evaluated using density functional theory (DFT) calculations at the B3LYP/6-31+G(d) level (see Sect. 2.2.4). The structures of $[PhO\cdot\text{-}H^+(H_2O)_{11,19}]$ were constructed by putting a PhO·-radical on a free OH group of the global minimum structures of $H^+(H_2O)_{11,19}$, which have been extensively studied experimentally and theoretically [76–78]. Cluster structures calculated for energy evaluation, shown in Fig. 2.13, have a separated radical-charge pair form. Although Kleinermanns et al. [74] reported that the PhO radical directly solvates the H_3O^+ moiety in the [phenol-$(H_2O)_4]^+$, cluster structures with $[PhO\cdot H_3O^+]$ core did not

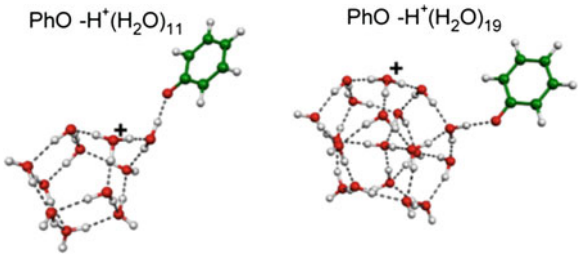

Fig. 2.13 Cluster structures of $[\text{phenol-}(H_2O)_{11,19}]^+$ ($[PhO\cdot\text{-}H^+(H_2O)_{11,19}]$) calculated for energy evaluation

survive during the geometry-optimization steps in our calculations of $[\text{phenol-}(H_2O)_{11}]^+$ and $[\text{phenol-}(H_2O)_{19}]^+$ because of the intracluster proton transfer. A similar situation was also seen in the $(H_2O)_n^+$ case (Chap. 5). Calculated adiabatic ionization energies, $[E(D_0) - E(S_0)]$, are 56,090 cm^{-1} for $\text{phenol-}(H_2O)_{11}$, and 54,935 cm^{-1} for $\text{phenol-}(H_2O)_{19}$. For $H^+(H_2O)_{11,19}$, experimental dissociation energy values are larger than 3,000 cm^{-1} [75]. According to the structural and chemical similarity, we assume $D(D_0)$ of $[\text{phenol-}(H_2O)_n]^+$ is the same as the reported dissociation energy of $H^+(H_2O)_n$. $D(S_0)$ is generally smaller than $D(D_0)$ because of the enhanced electrostatic interactions in the ionic state. Therefore, from Eqs. (2.1) and (2.2), the maximum Δn is evaluated to be 6 in both the cases..

It should be noted that the estimated value of Δn is based on hypothetical ionic cluster structures and calculated energies. This means an "exact" evaluation of Δn is hardly possible. Furthermore, Δn would be size-dependent because the ionization energy of clusters is size-dependent. This uncertainty is a limitation of the present moderately size-selective spectroscopy. Despite such uncertainty, observed spectra show clear size-dependence indicating good size-selectivity as shown in Sect. 2.3.

2.2.3.3 IR Spectral Measurements

For IR spectral measurement, the timing of the IR pulse was tuned to $\sim$50 ns prior to the UV pulse. Optical paths were then optimized by using reported IR transition of the phenol monomer. Re-adjustment of optical paths was not necessary for cluster spectroscopy.

Figure 2.14 shows the mass distribution of $[\text{phenol-}(H_2O)_n]^+$ produced by R2PI in the IR spectral measurement condition for $\text{phenol-}(H_2O)_{49}$. The red curve in Fig. 2.14 shows the mass distribution with IR irradiation, while the black curve shows it without IR irradiation. Figure 2.14 demonstrates that IR absorption causes predissociation of neutral clusters. The IR spectrum of the moderately size-selected cluster was measured as an ion-dip spectrum by monitoring the $[\text{phenol-}(H_2O)_n]^+$ ion intensity. Because IR predissociation of larger-sized clusters results in the fragmentation of the monitored ion channel $[\text{phenol-}(H_2O)_n]^+$, it causes an offset to the IR ion-dip spectrum of the cluster size of interest. To reduce such interference from larger-sized clusters, in every IR spectral measurement,

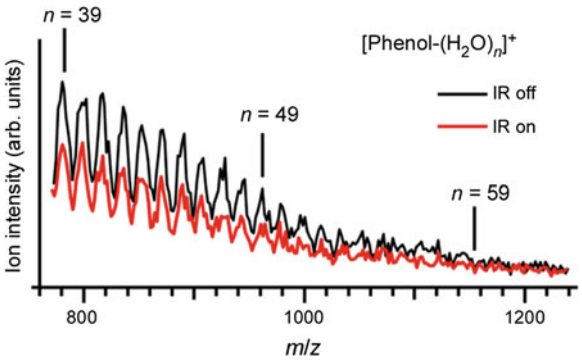

Fig. 2.14 Mass distribution of $[\text{phenol-}(H_2O)_n]^+$ produced by R2PI. The condition of the cluster production was optimized for IR spectral measurement of $\text{phenol-}(H_2O)_{49}$. The *red curve* shows the mass distribution with IR irradiation, while the *black* one shows the distribution without IR irradiation

we adjusted the cluster size distribution to reduce the clusters larger than those of interest by changing the jet expansion conditions. For example, the size distribution shown as the black curve in Fig. 2.14 is optimized for the IR measurement of $n = 49$.

2.2.4 Quantum Chemical Calculations

2.2.4.1 Calculation Procedures

For the detailed analyses of the cluster structures and their correlations with experimental spectra as well as their energies, DFT calculations were carried out using the B3LYP functional [79, 80] with the 6-31+G(d) basis set. The initial geometries of $(H_2O)_n$ were obtained from the reported low-lying minima or characteristic structures [7, 13, 16, 21, 81, 82], or otherwise they were manually constructed. Those of $\text{phenol-}(H_2O)_{n-1}$ were constructed by substituting one of the free hydrogen atoms in $(H_2O)_n$ to the phenyl group. All the cluster structures considered were fully geometry-optimized. In the geometry-optimizations, we typically used the redundant internal coordinates while the use of the distance matrix coordinates sometimes results in a better convergence.

At the stationary points, harmonic frequencies and IR intensities were calculated. All the calculated frequencies were scaled by a single factor of 0.9736, which was determined to reproduce the free OH stretching frequency of the cubic water octamer. There have been three experimental reports on the free OH frequency of cubic water octamer, i.e. $(H_2O)_8$, $\text{benzene-}(H_2O)_8$, and $\text{phenol-}(H_2O)_7$ [49, 54, 56, 63]. Here we employed the value of $\text{benzene-}(H_2O)_8$ [54], 3713.5 cm^{-1} as a reference experimental value to determine the scaling factor for

the following reasons: The previously reported spectrum of neat $(H_2O)_8$ suffers from low spectral resolution for precise determination of the free OH frequency. On the other hand, the resolution in the spectra of benzene-$(H_2O)_8$ is high enough. In addition, perturbation of the benzene ring on the free OH frequency is estimated to be negligible because free OH bands in both benzene-$(H_2O)_8$ and $(benzene)_2$-$(H_2O)_8$ show essentially the same frequency [56]. Though Kleinermanns and co-workers reported the free OH frequencies of 3711.5 cm^{-1} (D_{2d}-type) and 3710.5 cm^{-1} (S_4-type) for cubic phenol-$(H_2O)_7$, they employed atmospheric wavenumbers for their calibration [49, 50]. We confirm that their experimental values for phenol-$(H_2O)_7$ are in agreement with our calculated values, 3712.7 cm^{-1} (D_{2d}-type) and 3712.1 cm^{-1} (S_4-type) at the B3LYP/6-31+G(d) level of theory with the scaling factor of 0.9736 when the vacuum correction (addition ca. 0.8–1 cm^{-1} to atmospheric wavenumbers) is included.

The calculated stick spectrum was transformed into the continuous spectrum by using Lorentzian functions of 10 and 50 cm^{-1} full widths at half-maximum for the free and hydrogen-bonded OH stretches, respectively. Here, two bandwidths were used to take into account the lifetime-broadening induced by hydrogen bonding [83]. We note that this convolution was used only for convenience in the comparison with the simulated spectra and the values of the bandwidth have no rigorous physical meanings. The calculated free OH frequency reported in this study is the maximum of the single Lorentzian fitting of these overlapped multiple Lorentzian curves of the free OH bands. Therefore, we should note that we discuss the averaged behavior of the free OH bands. All the energy values include zero-point corrections. All the calculations in this study were carried out using the Gaussian 03 [84] and Gaussian 09 [85] programs. The cluster structures were drawn with the MOLEKEL program [86].

2.2.4.2 Detailed Analyses of Calculated Results

In spectroscopic studies of relatively small clusters, spectral analyses are sometimes carried out just by comparing calculated and experimental IR spectra. If the number of plausible isomers is small and their simulated spectra show isomer-dependent features, such an analysis works well to deduce cluster structures from the spectra. On the other hand, for large systems as in the present case, numerous stationary points should be possible [87, 88]. Furthermore, isomer-specific spectral features would be washed out. In these situations, isomer-based understanding is not possible. In this study, we tried to deduce structural trends of hydrogen bond networks, not exactly molecular-level structures. Calculated cluster structures and spectra were, then, analyzed in terms of the ring size distribution in networks and the coordination numbers of water molecules, both of which are introduced in Sect. 2.1 as the key factor to bridging the gap between the small clusters and bulky networks.

For the purpose of ring-size analyses, calculated structures are denoted by ring-size configuration, For example, the cubic water octamer (see Fig. 2.2) is represented by 4^6 (six 4-membered rings). For the coordination number analyses,

we determined coordination number distributions and spectral contributions of each coordination number according to the following procedures. First, using optimized geometry, atoms were grouped as the units of H_2O molecules. Second, the number of hydrogen bonds around each H_2O moiety (the coordination number) was counted. Here, the hydrogen bond was defined when O… H distance was longer than 1.3 and shorter than 2.3 Å. The definition of hydrogen bonding is thereby not sensitive to results. To estimate the distortion of networks, hydrogen bond angles were also calculated with the cosine formula. Thus determined coordination numbers were used for evaluating spectral contribution of each coordination number. For each normal mode, the magnitude of displacement of each atom was calculated and separately summed up according to each coordination number, to which each atom belonged. The calculated IR intensity of this mode was distributed to each coordination number according to the ratio of the resultant total values, i.e., relative weights of each coordination number. This band decomposition agreed with those reported so far for various sizes of $(H_2O)_n$ [5, 19, 89]. Figure 2.15a shows an example of such spectral decomposition for $(H_2O)_{48}$. The blue and red traces show the decomposition of the simulated spectrum (in black) to the 3- and 4-coordinated water components, respectively. We also tested simplified analyses, in which full IR intensity was assigned to the molecule with the largest displacement (Fig. 2.15b). This procedure resulted in similar trends to those of the detailed method, while vibrational mode was delocalized to several water molecules. For reasonability, we employed the former, detailed method in this study. All the above-mentioned procedures were automated by writing a Perl program.

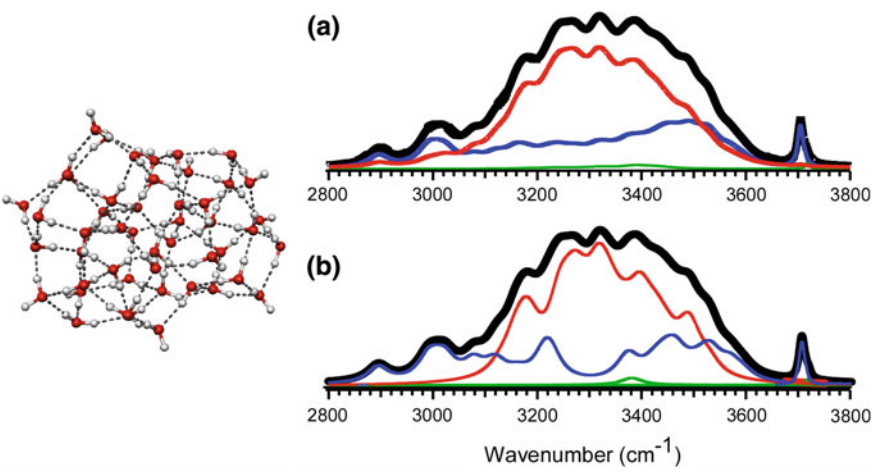

Fig. 2.15 Spectral decompositions for $(H_2O)_{48}$. **a** IR intensity is divided into each coordination number according to its contribution. **b** IR intensity is attributed to one water molecule showing largest displacement

2.2.4.3 Choice of the Calculation Method

As a result of recent progress in theory and also in computer technology, many theoretical methods are available today. Among them, *ab initio* and DFT calculations are powerful and therefore have become standard techniques to examine cluster structures and vibrational spectra. Of course, choice of the methods is important because calculated results often strongly depend on the chemical models employed. It should be noted that if someone strongly relies on calculated results (e.g., when someone compares calculated spectra of only a few isomers and concludes that the cluster structure is the one which shows the largest similarity in the spectral comparison), misinterpretations may occur [90, 91]. Benchmark studies, comparison of several methods and experimental results are required. For small hydrated clusters, Chang's group have carried out systematic calculations for hydrated clusters and compared the results of B3LYP functional, which is one of the most frequently-used methods in many chemical communities and *ab initio* MP2 [92–93]. They have shown both results are consistent with experimental results. Since their studies were conducted, lower-cost B3LYP calculations with the use of a scaling factor for harmonic frequencies have been applied to many hydrogen-bonded clusters of the broad size range ($\sim 6 \leq n \leq \sim 30$) and have successfully reproduced experimental IR spectra with acceptable computational costs [76, 92–95]. Furthermore, for large water clusters, high-level *ab initio*, such as MP2 and CCSD methods are not acceptable due to the computational limitations. Especially a frequency calculation based on these methods is highly time- and resource-consuming and only available with supercomputers. One of the largest systems ever to have been studied is $(H_2O)_{20}$ calculated at the MP2/CBS level [8, 9]. In this study, because we have to examine larger clusters and many structural isomers, the computational cost is an important factor to be considered. According to these considerations, we employed B3LYP here with a standard 6-31+G(d) basis set, which has also been tested previously [76, 92–94, 96].

It has been pointed out that the B3LYP functional is unable to treat systems in which the dispersion interaction plays vital roles. To evaluate the magnitude of the cooperative effect in interaction energy, the B3LYP functional may underestimate such interactions. Many new functionals (ωB97X-D [97], M06-2X [98, 99], etc.) [100] and empirical potentials (e.g., TTM2-F [101, 102]) have recently been proposed and they would be more accurate for energy evaluation due to better inclusion of the dispersion interactions and the long-range corrections. Evaluations of accuracy on vibrational frequencies with these methods are underway [8, 100]. As for frequency calculations of large-sized water clusters, the B3LYP functional with the use of a scale factor still seems to be a well-balanced method [103] between computational cost and accuracy (reliability).

2.2.4.4 Computational Resources

As mentioned above, the cost of the present method (B3LYP/6-31+G(d)) is relatively low. Even for the harmonic frequency calculation of a large system such as $(H_2O)_{48}$, only about 5 GB of memory is required. We then typically use home-built or commercially purchased low-cost computers. Typical specifications are as follows; Intel Core i7-2600 3.40 GHz (4 cores, 8 threads) CPU/DDR3-1333 $4 \times 4 = 16$ GB memory/2 TB SATA HDD/PGI or Intel compilers/Fedora 10 (64-bit) operating system. Of course, we had to calculate many cluster structures to characterize water networks and to find correlations between hydrogen bond network structures and spectral features. For this purpose, parts of the calculations were performed using supercomputing resources at Cyberscience Center, Tohoku University (TX7/i9610, up to 16 CPUs and 128 GB memory) and at the Research Center for Computational Science, Okazaki National Institutes of Natural Sciences (Altix4700, up to 8 CPUs and 64 GB memory).

2.3 Results

Figure 2.16 presents the observed IR spectra of size-selected phenol-$(H_2O)_n$ ($n = 19$–49) in the OH stretching region. Each spectrum includes the contribution of larger-sized clusters of phenol-$(H2O)_{n+\Delta n}$ ($0 \leq \Delta n \leq \sim 6$), but gradual changes of the spectral features prove the size-selectivity in the present spectroscopic scheme. The broadened absorption below 3,600 cm^{-1} is attributed to the hydrogen-bonded OH stretching vibrations, and the sharp band near 3,700 cm^{-1} is the free (dangling) OH stretching vibrations. Insets of Fig. 2.16 represent free and hydrogen-bonded OH stretching motions. The most prominent size-dependence is the decrease of relative intensity of the free band with increasing cluster size.

In previous studies on hydrated clusters, it has been shown that the behavior of free OH is sensitive to the surrounding hydrogen bonding environment. Figure 2.17 shows the expanded IR spectra of phenol-$(H_2O)_n$ ($n = 11$–49) in the free OH stretch region. All the spectra show a single band feature in this region. Since previous studies have revealed that $(H_2O)_{n \geq 6}$ clusters form 3-D structures consisting mainly of three-coordinated water molecules [60, 63], the band is assigned to the free OH stretching modes of such water molecules. Figure 2.17 shows a low-frequency shift of the band with increasing cluster size. Though this shift is somewhat slight, this is clear and reproducible. Observation of this shift also demonstrates that the moderate size selection of the spectral carrier is achieved by using photoionization mass spectrometry. The observed free OH frequencies are summarized in Table 2.1 and plotted in Fig. 2.18 (filled circles). Compared to cubic $(H_2O)_8$ [54], the magnitude of the shift amounts to 9 cm^{-1} in phenol-$(H_2O)_{49}$. We should note that the frequency shift observed in this study would lead to a similar one reported for the water nanoparticles in a much larger

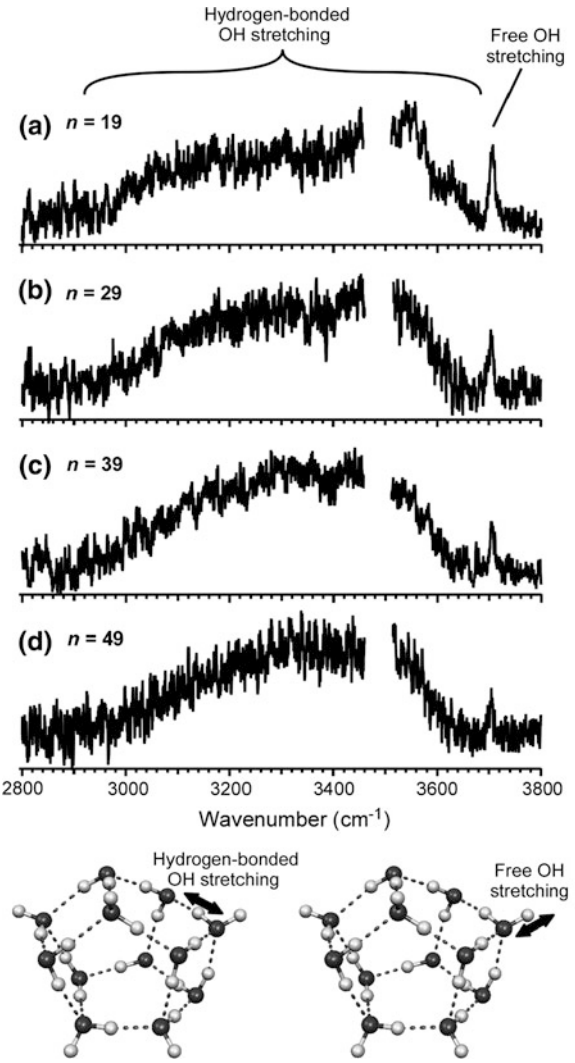

Fig. 2.16 Infrared (IR) spectra of moderately size-selected phenol-$(H_2O)_{n+\Delta n}$ in the OH stretching vibrational region. Each spectrum is obtained by monitoring the $[\text{phenol-}(H_2O)_n]^+$ cluster ion intensity. The size uncertainty (Δn) is estimated to be $0 \leq \Delta n \leq \sim 6$. The depletion depth of the ion intensity has been plotted. The gap in the spectra around 3,500 cm^{-1} is due to the depletion of the output of the IR light source (see Sect. 2.2)

size range ($n = \sim 200$–10^6) [5], though the relation between the shift and hydrogen bond network structures has not been clarified so far.

We should note that structural isomer selectivity is not achieved by the present IR spectroscopy. In a supersonic jet expansion, a number of energetically low-lying isomers would be formed especially for large-sized clusters, and we would observe an ensemble of such various structural isomers in the cluster size of interest. Moreover, there are many OH oscillators in each cluster. The free OH frequency in this experiment was determined by the maximum of the single Lorentzian fitting of overlapped free OH bands. Therefore, the observed spectra should reflect the averaged behavior of the water network structures in the ensemble of the clusters.

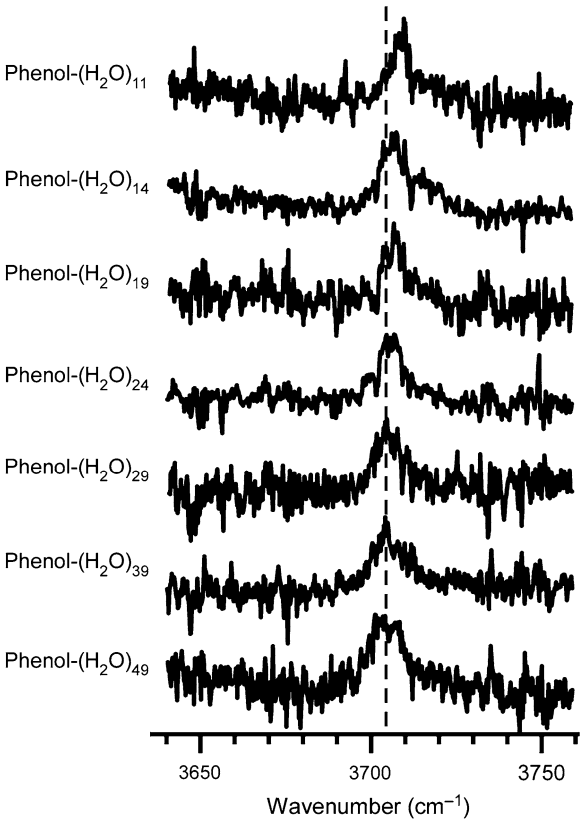

Fig. 2.17 Expanded IR spectra of phenol-$(H_2O)_n$ (n = 11–49) in the free OH stretch region. The *dashed line* is a visual guide

Table 2.1 Observed frequencies of free OH stretching bands in phenol-$(H_2O)_{n+\Delta n}$ (n = 11–49)

Cluster	Frequency (cm^{-1})
Benzene-$(H_2O)_8$[a]	3713.5
Phenol-$(H_2O)_{11}$	3709.0
Phenol-$(H_2O)_{14}$	3707.2
Phenol-$(H_2O)_{19}$	3706.8
Phenol-$(H_2O)_{24}$	3706.0
Phenol-$(H_2O)_{29}$	3705.1
Phenol-$(H_2O)_{39}$	3705.3
Phenol-$(H_2O)_{49}$	3704.5

These values are determined by single Lorentzian fitting of free OH bands. Each cluster size has an uncertainty of $0 \leq \Delta n \leq 6$. Errors in frequencies are within ± 1 cm^{-1}. The value of benzene-$(H_2O)_8$ is taken from previous work [54]

[a] From the Ref. [54]

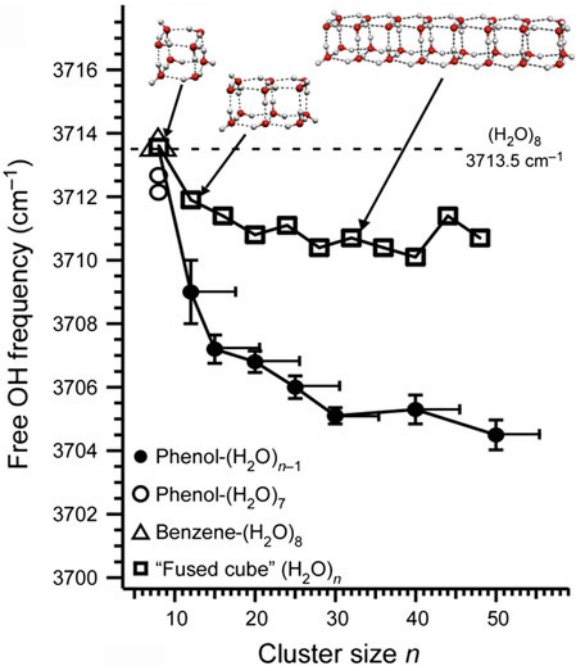

Fig. 2.18 Size-dependent free OH frequencies of phenol-$(H_2O)_{n-1}$ observed by IR spectroscopy (*filled circles*) and those of "fused cube" $(H_2O)_n$ obtained by calculations (*open squares*). Calculated values were obtained at the B3LYP/6-31+G(d) level, in which the harmonic frequencies were scaled by a factor of 0.9736. The *insets* show the "fused cube" structures. The *open circles* and *triangle* show the calculated free OH frequencies for phenol-$(H_2O)_7$ and benzene-$(H_2O)_8$, respectively, which agree with the corresponding experimental values

In the following sections, these spectral features are analyzed in terms of structural information of hydrogen bond networks.

2.4 Discussion

2.4.1 Analyses of Free OH Stretch Bands

2.4.1.1 Overview

To study the structures of hydrogen-bonded water networks, analyses of the free OH band would be a useful tool as OH band frequency is also very sensitive to hydrogen bonding environments [92, 94]. The free OH band is considered in this section. A lower free OH frequency is generally expected when the surrounding hydrogen bonds are stronger [94]. This is because the electron density on the free OH bond is slightly withdrawn by the neighboring proton donor molecules.

The observed low-frequency shift of $\sim 9\ cm^{-1}$ from $(H_2O)_8$ (Figs. 2.17 and 2.18) show that the hydrogen bonds increase their mean strengths as the network grows. In the following section, we discuss the origins of the enhancement of the hydrogen bond strengths.

2.4.1.2 Cooperative Effects in Water Clusters

One possible factor that may explain the enhancement of the hydrogen bond strength is cooperativity [83, 104]. The cooperative effect essentially originates from the non-additivity of the induction and dispersion terms. This effect means mutual enhancement among hydrogen bonds, and the magnitude of the effect increases with the number of surrounding hydrogen bonds. Figure 2.19 and its caption show an example schematic explanation of cooperativity in the case of the water trimer.

To evaluate the magnitude of the free OH frequency shifts caused by cooperativity, we performed DFT calculations at the B3LYP/6-31+G(d) level. We calculated the free OH vibrational frequencies of the "fused-cube" type structures (see insets in Fig. 2.18) [8, 9, 15], which are designed to indicate only the cooperative effects. These structures are extensions of cubic $(H_2O)_8$, increasing the number of hydrogen bonds while keeping the network motif, which consists only of 4-membered rings. In Fig. 2.18, filled circles show the observed free OH frequencies plotted versus the cluster sizes. The open circles and the triangle in Fig. 2.18 represent the calculated free OH frequencies for phenol-$(H_2O)_7$ and benzene-$(H_2O)_8$, respectively. These frequencies agree with the previously reported experimental values (see also Sect. 2.2) [49, 54]. Open squares in

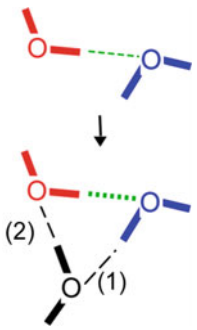

Fig. 2.19 Schematic explanation of cooperativity of hydrogen bonds. Upon trimer formation, two hydrogen bonds (*1* and *2*) are formed. This enhances the strength of the hydrogen bond (*green*) for the following reason. Due to the hydrogen bond (*1*) formation, electron density around the O atom in the H_2O (*blue*) increases (hydrogen bonding can be interpreted as the charge transfer from the lone pair to the anti-bonding orbital). On the other hand, hydrogen bonding (*2*) decreases electron density around the O atom in the H_2O (*red*). As a result, polarization of the original water pair (*blue–red pair*) is enhanced. This leads to the enhancement of the intermolecular interaction (the *green hydrogen bond*)

Fig. 2.18 show the calculated free OH frequencies of "fused-cube" clusters. Calculated frequencies of cubic $(H_2O)_n$ show the low-frequency shift similar to the experimental observations. However, the magnitude of the shifts in the "fused-cube" series is estimated to be much smaller than that in the experimentally observed series. These results suggest that cooperativity accounts for only a part of the observed low-frequency shifts.

It has been pointed out that the B3LYP functional is unable to treat systems in which the dispersion interaction plays vital roles [105]. However, in frequency calculations (at least for scaled harmonic frequencies), the B3LYP functional with a suitable basis set seems to be the best-balanced method between the computational cost and accuracy for large-sized clusters, as mentioned in Sect. 2.2. Furthermore, *ab initio* calculations for cubic $(H_2O)_8$ and $(H_2O)_{20}$ at the MP2/aug-cc-pVDZ level were reported by Xantheas and co-workers [9, 106]. These high level calculations, however, predict the low-frequency shift of $\sim 1\ cm^{-1}$ from $(H_2O)_8$ to $(H_2O)_{20}$. This small shift suggests that the present DFT calculations do not significantly underestimate the frequency shift due to the cooperative effect.

2.4.1.3 Structural Strains in Water Clusters

Another possible factor for the low-frequency shifts of the free OH bands is the change of the hydrogen bond network structural motif, which also affects hydrogen bond strength. To clarify this point, we calculated structures of small ring-type $(H_2O)_n$ (n = 3–8). Figure 2.20 shows their structures with the averaged hydrogen

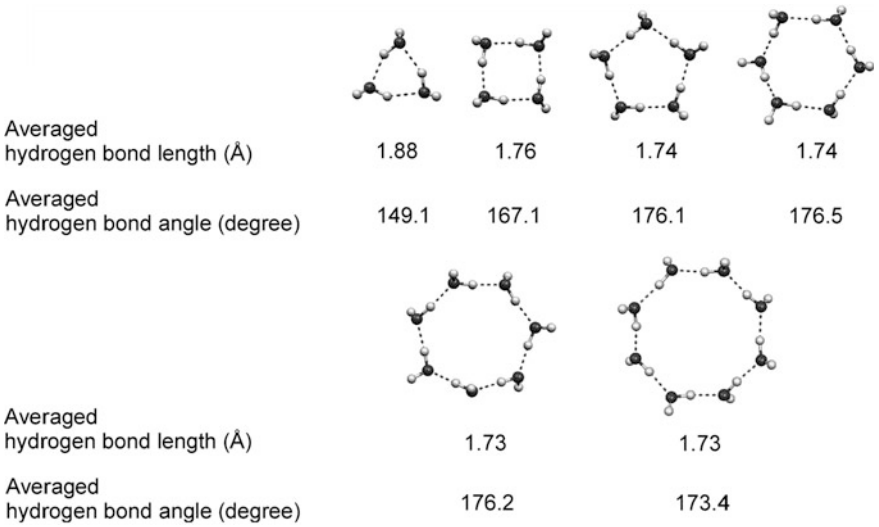

Fig. 2.20 Calculated hydrogen bond parameters of various ring type $(H_2O)_n$. These structures are optimized at the B3LYP/6-31+G(d) level. Hydrogen bonds are clearly weaker in the 3- and 4-membered rings as indicated distorted angles and longer intermolecular distances

bond angles and hydrogen bond lengths. It is clear that hydrogen bonds are weaker in the 3- and 4-membered rings as indicated by distorted hydrogen bond angles and longer hydrogen bond lengths. On the basis of the DFT calculations for the small-sized $(H_2O)_n$ ($n \leq 10$), Jiang et al. [94] have shown the hydrogen bond distortion affects the free OH frequency. To evaluate such a structural effect on the free OH frequency in larger systems, we calculated model structures of larger clusters. Figure 2.21 shows some of the characteristic model structures of $(H_2O)_{18–20}$ and those of corresponding phenol-$(H_2O)_{17–19}$ with their frequencies of the free OH bands simulated using DFT. The frequencies of phenol-$(H_2O)_{17–19}$ of the same hydrogen bond network are presented in parentheses, and they show the perturbation caused by the phenyl group is less than 1.5 cm^{-1} for the free OH frequency. To clarify the correlation between the hydrogen bonding environment and the OH frequency, Fig. 2.22 contains a summary of calculated results on hydrogen bond networks of these four different types. Among these structures (in Figs. 2.21 and 2.22), the "fused-cube" consists only of 4-membered rings and has highly distorted hydrogen bonds, the same as cubic $(H_2O)_8$. The "prism" structure, which consists of 4- and 5-membered rings, has been predicted to be the energy global minimum in $(H_2O)_{20}$ by the various theoretical studies including high level *ab initio* calculations. The "dodecahedral cage" consists of twelve 5-membered rings and can be regarded as a partial structure of clathrate hydrates. "Hexagonal

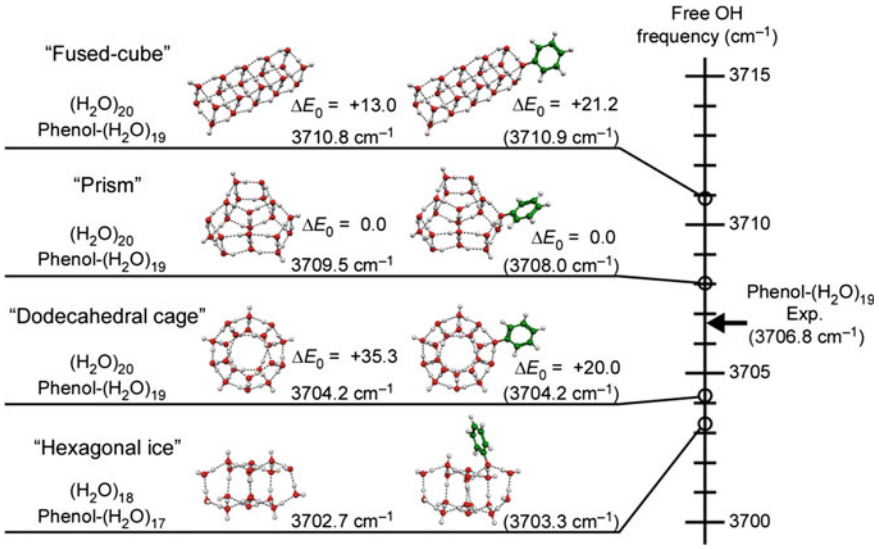

Fig. 2.21 Free OH stretching frequencies of the characteristic cluster structures of $(H_2O)_{18–20}$ and corresponding phenol-$(H_2O)_{17–19}$. For $(H_2O)_{20}$ and phenol-$(H_2O)_{19}$, relative energies at the vibrational zero-point level (ΔE_0) were also shown in kJ/mol. All cluster structures, their harmonic frequencies, and relative energies were calculated at the B3LYP/6-31+G(d) level. Harmonic frequencies were scaled by a factor of 0.9736. In "hexagonal ice", free OH stretching modes of the two-coordinated water molecules and the π-hydrogen bonded OH bond were excluded from the evaluation of the free OH frequency

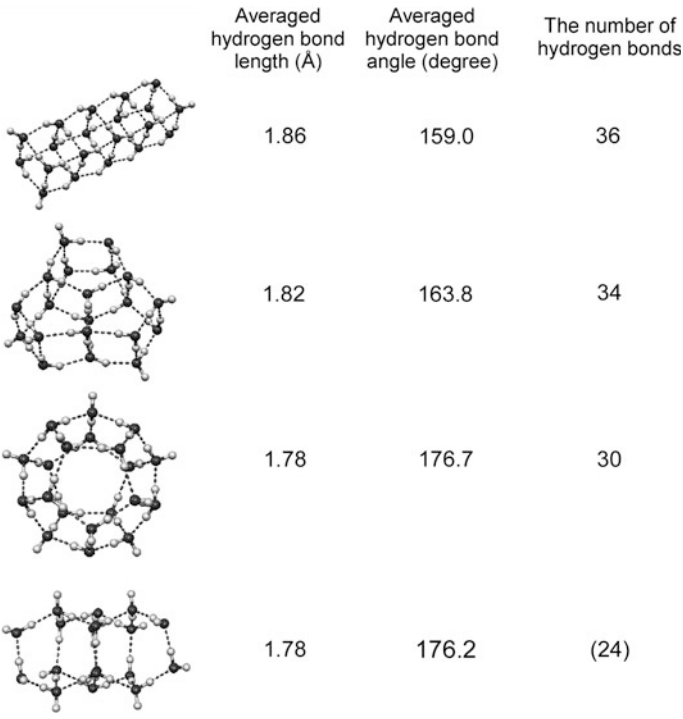

Fig. 2.22 Summary of calculated results of the four $(H_2O)_{18–20}$ structures shown in Fig. 2.21. Note that the bottom ("hexagonal ice") is smaller system than the others and therefore, the number of hydrogen bonds should also be small

ice" has a very similar network structure to the crystalline hexagonal ice, consisting only of 6-membered rings. The distortions of hydrogen bonds in the "dodecahedral cage" and "hexagonal ice" structures are much fewer: the hydrogen bond angles are straighter (O–H…O angle is 170–180°) in the 5- and 6-membered rings than those in the 4-membered rings (O–H…O angle is 140–170°) as indicated in Fig. 2.22. Figures 2.21 and 2.22 show the clear correlation between the magnitude of the hydrogen bond distortions and the free OH frequencies. The free OH frequency of the most strained "fused-cube" is predicted to be the highest value, 3710.8 (3710.9 cm^{-1} in corresponding phenol-$(H_2O)_n$), and those of the less strained "dodecahedral cage" and "hexagonal ice" are 3704.2 (3704.2) and 3702.7 (3703.3 cm^{-1}), respectively. The free OH frequency of "prism" is located in between those of the "fused-cube" and "dodecahedral cage" (or "hexagonal ice"), reflecting the coexistence of the 4- and 5-membered ring motifs. It should be noted that the frequency calculations at the MP2/aug-cc-pVDZ level also show a similar correlation.

The experimental frequency of phenol-$(H_2O)_{19}$ is located between "prism" and "dodecahedral". This location suggests the observed water networks of $n \sim 20$ consist not only of 4-membered rings but also of 5- and/or 6-membered rings.

At this time, the 4-membered ring motif is no longer exclusive and the networks are being replaced by more relaxed structural motifs.

Because the observed experimental spectrum measured by monitoring [phenol-$(H_2O)_{19}$]$^+$ includes the contribution of phenol-$(H_2O)_{20,21\ldots}$, we also carried out similar analyses for these sizes. Figure 2.23 shows optimized structures of $(H_2O)_{20–22}$. These structures have been reported as low-lying minima in previous theoretical studies [13, 21]. In Fig. 2.23, some structures with higher frequencies ($>\sim$3,710 cm^{-1}, for example) clearly include more 4-membered rings than others. The above-mentioned correlation is therefore confirmed.

For further confirmation, similar analyses were carried out for the larger clusters. Figure 2.24 shows characteristic structures of $(H_2O)_{48}$ with their free OH frequencies and hydrogen bond parameters. The frequencies of corresponding phenol-$(H_2O)_{47}$ are also shown in parentheses. These calculations show the same trend as $(H_2O)_{20}$. The free OH frequency of the most strained "fused-cube" structure is evaluated to be the highest while those of more relaxed "hexagonal prism" and "filled cage" are evaluated to be lower. As is in $(H_2O)_{18–20}$, the frequency of "fused-cube" is much higher than the experimental value, meaning that the 4-membered ring (cubic) motif is not exclusive in the hydrogen bond network. In

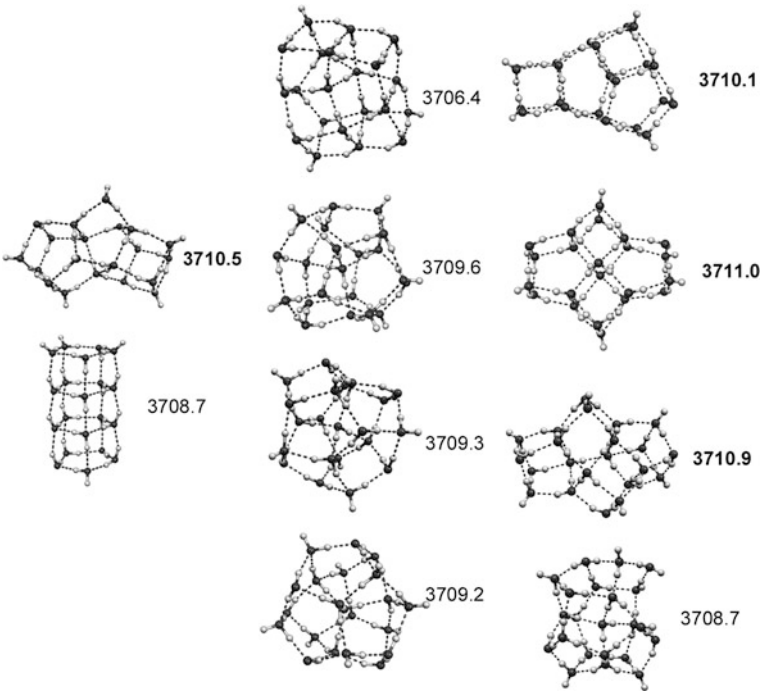

Fig. 2.23 Optimized cluster structures of $(H_2O)_{20–22}$ with the calculated free OH frequency. We can see a clear trend that the structures with 3,710 cm^{-1} or higher frequency contain many 4-membered rings than the others

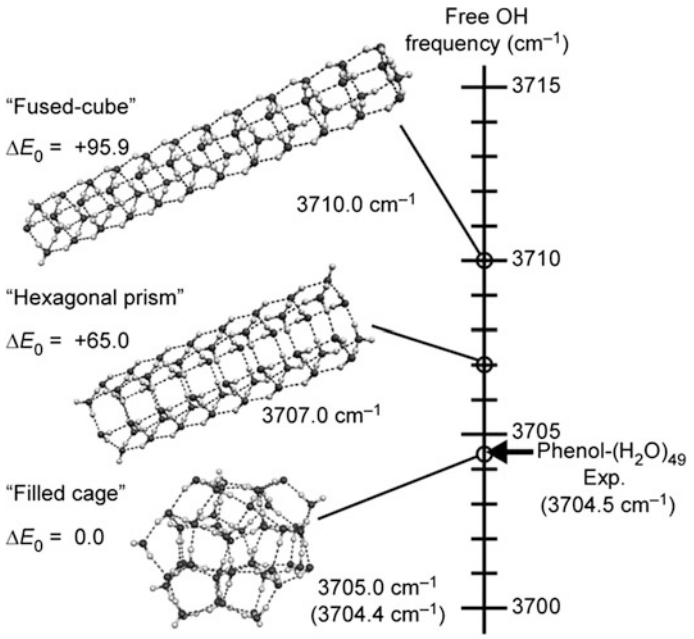

Fig. 2.24 Free OH stretching frequencies and relative energies (ΔE_0) in kJ/mol of the characteristic cluster structures of $(H_2O)_{48}$. Parameters of the hydrogen bond environment are also indicated. Frequencies of corresponding phenol-$(H_2O)_{47}$ are also shown in *parentheses*. Each cluster structure and its energy and harmonic frequencies were calculated at the B3LYP/6-31+G(d) level and all the harmonic frequencies were scaled by a factor of 0.9736

the case of $(H_2O)_{20}$ in Fig. 2.21, the frequency of the "prism" structure is nearest to the experimental value. On the other hand, the free OH frequency of the "hexagonal prism" in $(H_2O)_{48}$ no longer agrees with the experimental value, while the more relaxed "filled cage", which is the reported global minimum on the TIP4P potential energy surface [7], is in good agreement with the observation. The contribution of the 4-membered rings in this "filled cage" was reported to be only 18 %, and the 5- and 6-membered rings are clearly dominant [7].

These results indicate that the hydrogen bond network structure develops from the highly strained 4-membered ring motif to the more relaxed motifs of 5- and 6-membered rings with the growth of the network, and the low-frequency shift of the free OH stretching band originates from the gradual transition of the structural motifs as well as the hydrogen bond cooperativity. This interpretation is consistent with the structural trends of hydrogen bond network development, which have been predicted by theoretical calculations. At $n = 8$, the 4-membered rings are exclusive (100 %). With increasing size, at $n \sim 20$, the contributions of the 5- or 6-membered rings become necessary to reproduce the experimental frequency (in the plausible "prism" structure, the 4-membered rings still take over 67 % of the network). Then, at $n \sim 50$, the contribution of the 4-membered rings is estimated to be $\sim$20 %.

Because the experimental and the calculated free OH frequency shifts are somewhat slight (within 10 cm^{-1}), accuracy of the calculated frequencies is critical. Actually, the absolute accuracy of the scaled harmonic frequencies based on the B3LYP/6-31+G(d) level have been estimated to be only $\sim$20 cm^{-1}. However, we optimized the scaling factor for free OH stretching frequencies and essentially focused on the relative frequencies. In this case, the reliability of the present calculations will be higher. Furthermore, the MP2/aug-cc-pVDZ level calculations of $(H_2O)_{20}$ also show a similar correlation between the hydrogen bond distortions and free OH frequencies. The consistency of these higher-level calculations and our DFT calculations suggests that such correlation is a general trend and that the experimental frequency shift, more or less, is accounted for by the relaxation of the hydrogen bond distortions. Of course, further discussion will be done by fine anharmonic frequency calculations, which will be available in the near future.

2.4.1.4 Further Discussion of Free OH Bands

In addition to the effects of the hydrogen bond distortion, Jiang et al. [94] have reported another factor in the free OH frequency shift. On the basis of the DFT calculations for model clusters, they showed that neighboring 4-coordinated waters lower the free OH frequency relative to neighboring 3-coordinated waters. The present calculations are helpful to estimate the magnitude of such a coordination environment effect in the larger-sized region. In Fig. 2.21, the free OH bond in the "dodecahedral cage" is surrounded by three 3-coordinated waters and the "fused-cube" is surrounded by two 3-coordinated and one 4-coordinated waters. However, the free OH frequency in the "fused-cube" is calculated to be higher than that in "dodecahedral cage". These calculations suggest that the network distortion is more effective than the neighboring water coordination effect in the size region of $n \sim 20$.

In the present DFT analyses, we selected some characteristic cluster structures to examine the correlation between the structural strain and the free OH frequency. However, it should be noted that there exist large numbers of structural isomers in the observed sizes, and only their averaged trend associated with size is reflected in the observed frequency. No specific isomer structures can be identified in the present study, but only the general trend in the network development is inferred. Though the present calculations show a clear correlation between the observed frequency shift and the structural strain in the water network, extensive sampling of isomer structures or global search of potential energy surfaces [88] is requested for unequivocal proof of the origin of the shift. Such calculations for clusters of $n > \sim 10$ are very time-consuming, and are beyond the scope of the present study.

Finally, we comment on the effect of the cluster temperature. Finite (and undefined) temperature or internal energy of clusters affects their preferential structures. In conventional IR–UV double resonance spectroscopy of a jet-cooled neutral cluster, only a few energetically low-lying isomers are ordinarily

considered, because the low temperature (or specific internal energy) of the cluster can be ensured by sharp vibronic bands in its electronic spectrum. In the present experiment, broadened electronic spectra of the large-sized clusters prevent us from evaluating the cluster temperature. In addition, the optimization of the size distribution in each IR measurement might cause the size dependence of the temperature of the observed clusters. Though the temperature of the clusters is an ambiguous factor in the present experiment, we infer that the size dependence of the cluster temperature is not a major origin of the observed OH frequency shift for the following reasons: (i) The observed shift is reproducible irrespective of arbitrary optimization of the jet condition and size distribution. (ii) For both $(H_2O)_{20}$ and $(H_2O)_{48}$, the calculated free OH frequencies based on the reported energetically global minimum structures are in agreement with the experimental values. These agreements imply the observed IR spectra of both $n \sim 20$ and ~ 50 reflect low-lying cluster structures. (iii) A similar low-frequency shift has been found for ice nanoparticles of a much larger size range ($n = 200$–10^6) prepared by a collisional cooling cell [5]. The shift reported here would lead to this ice nanoparticle behavior.

2.4.2 Analyses of Hydrogen-Bonded OH Stretch Bands

2.4.2.1 Intensity Ratio

Coordination numbers of water molecules are also important factors in characterizing hydrogen-bonded water networks. The IR spectra of phenol-$(H_2O)_n$ in Fig. 2.16 show that the intensity of the free OH band relative to that of the hydrogen-bonded OH band gradually decreases with increasing n. Because 4-coordinated waters have no free OH, the observed free OH band is mainly attributed to 3-coordinated waters. The decrease of the free OH band intensity is therefore a signature of the increase of 4-coordinated waters.

2.4.2.2 Contribution from Each Coordination Number

Corresponding to this indication of 4-coordinated waters, spectral contributions of the 4-coordinated waters are expected to appear in the hydrogen-bonded OH stretch region. In the spectrum of $n = 19$, the hydrogen-bonded OH band is very broad and it shows the almost flat intensity distribution in the range of 3,000–3,600 cm^{-1}. With increasing cluster size, the absorption at around 3,200–3,500 cm^{-1} gradually rises, while the intensities in both the edge regions of the hydrogen-bonded OH band are relatively suppressed. In the spectrum of $n = 49$, the band finally forms a broad peak at around 3,350 cm^{-1}. Because this spectral change in the hydrogen bonded OH band correlates with the suppression of the free OH band, it is reasonable to attribute the rise of the absorption centered at

$\sim$3,350 cm^{-1} to the increase of 4-coordinated waters. Similar trends have been also reported for average size-estimated water clusters [5].

To provide further confirmation of the contribution of 4-coordinated waters, a similar comparison was carried out among the observed IR spectrum of phenol-$(H_2O)_{49}$ and simulated ones of $(H_2O)_{48}$, as shown in Fig. 2.25a, c. The global minimum structure of $(H_2O)_{48}$ under the TIP4P potential has been reported by Kazimirski et al. [7]. We re-optimized this structure at B3LYP, and the resulting spectral simulation is shown in Fig. 2.25c (the same structure as in Fig. 2.24). To highlight the feature of 3-coordinated waters, we also constructed a model structure consisting only of 3-coordinated waters. This structure became a "hollow-cage type", shown with its simulated spectrum in Fig. 2.25b. The calculated spectrum (b) shows broad absorption in 3,000–3,600 cm^{-1} without a single prominent maximum. This reveals that the peak at $\sim$3,350 cm^{-1} in the observed spectrum (a) cannot be rationalized only with 3-coordinated waters. The free OH band in spectrum (b) is also too intense relative to the hydrogen-bonded OH band, in comparison with spectrum (a). On the other hand, the spectrum in Fig. 2.25c

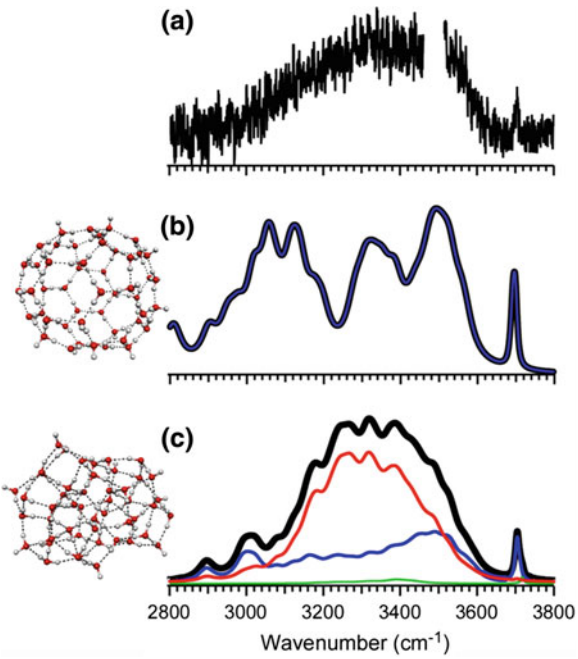

Fig. 2.25 Comparison between (**a**) observed IR spectrum of phenol-$(H_2O)_{49}$ and (**b**, **c**) simulated spectra of $(H_2O)_{48}$. Simulated spectrum (**b**) is based on all 3-coordinated water structures shown in the *inset*. Spectrum (**c**) is given by the global minimum structure at the TIP4P potential, which is taken from the previous work [7]. Both the structures are (re-)optimized at the B3LYP/6-31+G(d) level. In the simulations, the *black line* represents the IR spectrum, and the *green*, *blue*, and *red traces* are a decomposition of the spectrum to the 2-, 3-, and 4-coordinated water components, respectively

shows qualitative agreement with spectrum (a): a peak appears at around 3,300 cm^{-1}, and the relative intensity of the free OH stretch band is similar to the observed one. The global minimum structure of $(H_2O)_{48}$ is constructed of 27, 20, and 1 water molecules in the 4-, 3-, and 2-coordinated sites, respectively. The contribution of the 4-coordinated waters is dominant in the simulated spectrum, and it causes the apparent maximum in the hydrogen-bonded OH region. These results show that the absorption maximum centered at $\sim$3,350 cm^{-1} is reasonably interpreted as a spectral signature of 4-coordinated water sites in the neutral water clusters of $n \leq \sim 50$.

For further confirmation of the 4-coordinated water band, we also simulated spectra of isomers of other sizes, which are used in discussion of free OH behavior or previously reported minima. The band decompositions (Fig. 2.26) show similar trends as that of $(H_2O)_{48}$, showing the generality of coordination number dependent frequencies. This result also supports the formation of 4-coordinated water molecules in the present size range.

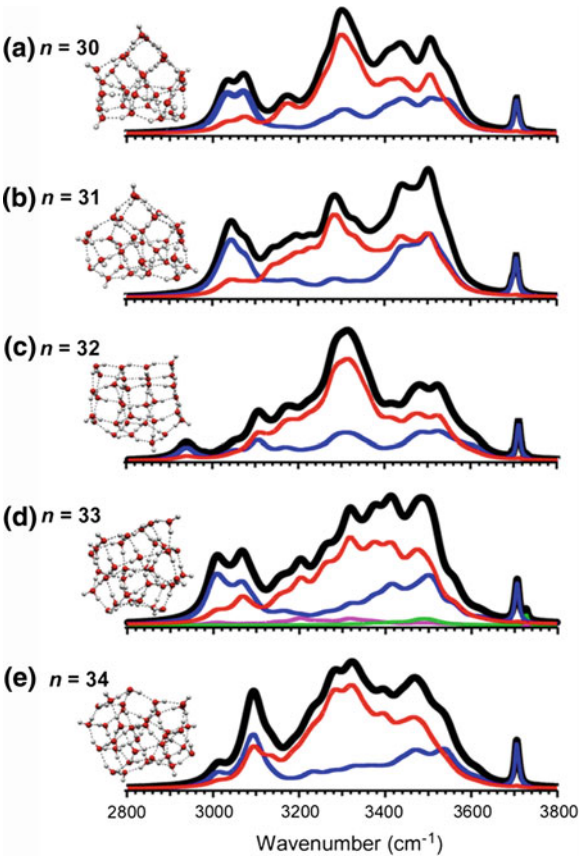

Fig. 2.26 **a** – **e** Comparison between experimental spectra and simulated spectra for many cluster structures of $(H_2O)_n$ (n = 30-34)

2.4.2.3 Further Discussion of Hydrogen-Bonded OH Bands

Formation of 4-coordinated sites is closely related to formation of the interior moiety in water clusters. This is an important step in the development of hydrogen bond networks from water clusters to bulk water, and the network evolution in this size range ($n < \sim 50$) corresponds to its very early stage. The hydrogen-bonded OH stretch frequency of ice (Ih) is 3,200 cm^{-1} [83, 107, 108], much lower than in the present observations. This means that the OH frequency of 4-coordinated sites in the clusters will show further lowering with the expansion of the network among 4-coordinated waters. Such a shift has been observed in much larger-sized clusters/ice nano particles [5, 109].

2.5 Conclusion

To analyze hydrogen bond network structures consisting of tens of water molecules, we measured moderately size-selective IR spectra of large, labeled water clusters phenol-$(H_2O)_n$ in the OH stretch region. The observed spectral features were analyzed in terms of hydrogen bond ring size motifs and coordination numbers of water molecules. The detailed analyses of the free OH band indicated that the observed low-frequency shift originates from the cooperativity of hydrogen bonds and the structural development from the highly strained 4-membered ring motif to the more relaxed 5- and 6-membered ring motifs. The suppression of free OH band intensity with an increase of n represents the increase of the abundance of 4-coordinated waters. The rise of the absorption maximum of the hydrogen-bonded OH stretch band at $\sim$3,350 cm^{-1} can also be attributed to 4-coordinated water sites. The characterized structural trends are bridging the gap between the small clusters and bulky networks. We note that we did not determine the exact or specific structures. As numerous structures should coexist in such a large system and many of them are not distinguishable with spectroscopy, the present approach toward averaged behavior seems helpful in characterizing and understanding hydrogen bond networks. In this study, we discussed the correlation between spectral features and structures by calculating only a few characteristic structures. If many more structures were systematically used, more detailed information could be obtained. Owing to recent progress in computational chemistry, such calculations will become possible in the near future. In such a procedure, we hope that our approach, which checks the coordination number and ring size distribution, will also be useful for evaluating the calculated results. We also expect that the present characterization method of hydrogen bond networks may be applicable to more complicated, condensed phase water.

References

1. R.H. Page, M.F. Vernon, Y.R. Shen, Y.T. Lee, Chem. Phys. Lett. **141**, 1–6 (1987)
2. U. Buck, F. Huisken, Chem. Rev. **100**, 3863–3890 (2000)
3. L.M. Goss, S.W. Sharpe, T.A. Blake, V. Vaida, J.W. Brault, J. Phys. Chem. A **103**, 8620–8624 (1999)
4. C. Steinbach, P. Andersson, J.K. Kazimirski, U. Buck, V. Buch, T.A. Beu, J. Phys. Chem. A **108**, 6165–6174 (2004)
5. V. Buch, S. Bauerecker, J.P. Devlin, U. Buck, J.K. Kazimirski, Int. Rev. Phys. Chem. **23**, 375–433 (2004)
6. P. Andersson, C. Steinbach, U. Buck, Euro. Phys. J. D. **24**, 53–56 (2003)
7. J.K. Kazimirski, V. Buch, J. Phys. Chem. A **107**, 9762–9775 (2003)
8. G.S. Fanourgakis, E. Apra, S.S. Xantheas, J. Chem. Phys. **121**, 2655–2663 (2004)
9. G.S. Fanourgakis, E. Apra, W.A. de Jong, S.S. Xantheas, J. Chem. Phys. **122**, 134304 (2005)
10. A. Lagutschenkov, G.S. Fanourgakis, G. Niedner-Schatteburg, S.S. Xantheas, J. Chem. Phys. **122**, 194310 (2005)
11. S. Bulusu, S. Yoo, E. Apra, S. Xantheas, X.C. Zeng, J. Phys. Chem. A **110**, 11781–11784 (2006)
12. B. Hartke, Angew. Chem. Int. Ed. **41**, 1468–1487 (2002)
13. B. Bandow, B. Hartke, J. Phys. Chem. A **110**, 5809–5822 (2006)
14. L.S. Sremaniak, L. Perera, M.L. Berkowitz, J. Chem. Phys. **105**, 3715–3721 (1996)
15. C.J. Tsai, K.D. Jordan, J. Phys. Chem. **97**, 5208–5210 (1993)
16. D.J. Wales, M.P. Hodges, Chem. Phys. Lett. **286**, 65–72 (1998)
17. H. Kabrede, R. Hentschke, J. Phys. Chem. B **107**, 3914–3920 (2003)
18. A. Lenz, L. Ojamae, Phys. Chem. Chem. Phys. **7**, 1905–1911 (2005)
19. A. Lenz, L. Ojamäe, J. Phys. Chem. A **110**, 13388–13393 (2006)
20. A. Lenz, L. Ojamäe, Chem. Phys. Lett. **418**, 361–367 (2006)
21. H. Takeuchi, J. Chem. Inf. Model. **48**, 2226–2233 (2008)
22. S. Kazachenko, A.J. Thakkar, Chem. Phys. Lett. **476**, 120–124 (2009)
23. G. Scoles (ed.), *Atomic and Molecular Beam Methods* (Oxford University Press, New York, 1988)
24. Electron ionization is an universal detection method, however, overlap of electron beam and IR light, which is for spectroscopy, is not easily achieved. This is because the focusing of electron beam has many difficulties such as repulsion due to the charge. Generally, when the ionization is achieved by photons, an overlapping of the ionization light and the IR light is relatively easy
25. H. Shinohara, N. Nishi, N. Washida, J. Chem. Phys. **84**, 5561–5567 (1986)
26. I.B. Muller, L.S. Cederbaum, J. Chem. Phys. **125**, 204305 (2006)
27. L. Belau, K.R. Wilson, S.R. Leone, M. Ahmed, J. Phys. Chem. A **111**, 10075–10083 (2007)
28. E.S. Wisniewski, J.R. Stairs, A.W. Castleman Jr, Int. J. Mass Spectrom. **212**, 273–286 (2001)
29. P.P. Radi, P. Beaud, D. Franzke, H.M. Frey, T. Gerber, B. Mischler, A.P. Tzannis, J. Chem. Phys. **111**, 512–518 (1999)
30. H. Abe, N. Mikami, M. Ito, J. Phys. Chem. **86**, 1768–1771 (1982)
31. A. Oikawa, H. Abe, N. Mikami, M. Ito, J. Phys. Chem. **87**, 5083–5090 (1983)
32. K. Fuke, K. Kaya, Chem. Phys. Lett. **94**, 97–101 (1983)
33. R.J. Lipert, S.D. Colson, J. Chem. Phys. **89**, 4579–4585 (1988)
34. R.J. Lipert, S.D. Colson, J. Phys. Chem. **93**, 135–139 (1989)
35. R.J. Lipert, S.D. Colson, Chem. Phys. Lett. **161**, 303–307 (1989)
36. R.J. Lipert, S.D. Colson, J. Chem. Phys. **92**, 3240–3241 (1990)
37. R.J. Lipert, S.D. Colson, J. Phys. Chem. **94**, 2358–2361 (1990)

38. G. Reiser, O. Dopfer, R. Lindner, G. Henri, K. Mullerdethlefs, E.W. Schlag, S.D. Colson, Chem. Phys. Lett. **181**, 1–4 (1991)
39. O. Dopfer, G. Reiser, K. Mullerdethlefs, E.W. Schlag, S.D. Colson, J. Chem. Phys. **101**, 974–989 (1994)
40. R.J. Stanley, A.W. Castleman, J. Chem. Phys. **94**, 7744–7756 (1991)
41. G.V. Hartland, B.F. Henson, V.A. Venturo, P.M. Felker, J. Phys. Chem. **96**, 1164–1173 (1992)
42. S. Tanabe, T. Ebata, M. Fujii, N. Mikami, Chem. Phys. Lett. **215**, 347–352 (1993)
43. T. Watanabe, T. Ebata, S. Tanabe, N. Mikami, J. Chem. Phys. **105**, 408–419 (1996)
44. T. Ebata, A. Fujii, N. Mikami, Int. Rev. Phys. Chem. **17**, 331–361 (1998)
45. M. Gerhards, K. Kleinermanns, J. Chem. Phys. **103**, 7392–7400 (1995)
46. G. Berden, W.L. Meerts, M. Schmitt, K. Kleinermanns, J. Chem. Phys. **104**, 972–982 (1996)
47. M. Gerhards, M. Schmitt, K. Kleinermanns, W. Stahl, J. Chem. Phys. **104**, 967–971 (1996)
48. W. Roth, M. Schmitt, C. Jacoby, D. Spangenberg, C. Janzen, K. Kleinermanns, Chem. Phys. **239**, 1–9 (1998)
49. C. Janzen, D. Spangenberg, W. Roth, K. Kleinermanns, J. Chem. Phys. **110**, 9898–9907 (1999)
50. A. Lüchow, D. Spangenberg, C. Janzen, A. Jansen, M. Gerhards, K. Kleinermanns, Phys. Chem. Chem. Phys. **3**, 2771–2780 (2001)
51. R.H. Page, Y.R. Shen, Y.T. Lee, J. Chem. Phys. **88**, 5362–5376 (1988)
52. T.S. Zwier, Annu. Rev. Phys. Chem. **47**, 205–241 (1996)
53. R.N. Pribble, T.S. Zwier, Science **265**, 75–79 (1994)
54. C.J. Gruenloh, J.R. Carney, C.A. Arrington, T.S. Zwier, S.Y. Fredericks, K.D. Jordan, Science **276**, 1678–1681 (1997)
55. R.N. Pribble, F.C. Hagemeister, T.S. Zwier, J. Chem. Phys. **106**, 2145–2157 (1997)
56. C.J. Gruenloh, J.R. Carney, F.C. Hagemeister, C.A. Arrington, T.S. Zwier, S.Y. Fredericks, J.T. Wood III, K.D. Jordan, J. Chem. Phys. **109**, 6601–6614 (1998)
57. C.J. Gruenloh, J.R. Carney, F.C. Hagemeister, T.S. Zwier, J.T. Wood III, K.D. Jordan, J. Chem. Phys. **113**, 2290–2303 (2000)
58. N. Pugliano, R.J. Saykally, Science **257**, 1937–1940 (1992)
59. J.D. Cruzan, L.B. Braly, K. Liu, M.G. Brown, J.G. Loeser, R.J. Saykally, Science **271**, 59–62 (1996)
60. K. Liu, M.G. Brown, C. Carter, R.J. Saykally, J.K. Gregory, D.C. Clary, Nature **381**, 501–503 (1996)
61. K. Liu, M.G. Brown, J.D. Cruzan, R.J. Saykally, Science **271**, 62–64 (1996)
62. K. Liu, J.D. Cruzan, R.J. Saykally, Science **271**, 929–933 (1996)
63. U. Buck, I. Ettischer, M. Melzer, V. Buch, J. Sadlej, Phys. Rev. Lett. **80**, 2578 (1998)
64. I.V. Hertel, C. Hüglin, C. Nitsch, C.P. Schulz, Phys. Rev. Lett. **67**, 1767–1770 (1991)
65. R.M. Forck, I. Dauster, Y. Schieweck, T. Zeuch, U. Buck, M. Oncak, P. Slavicek, J. Chem. Phys. **132**, 221102 (2010)
66. C. Steinbach, U. Buck, J. Phys. Chem. A **110**, 3128–3131 (2005)
67. H.T. Liu, J.P. Müller, N. Zhavoronkov, C.P. Schulz, I.V. Hertel, J. Phys. Chem. A **114**, 1508–1513 (2010)
68. K. Hashimoto, K. Morokuma, J. Am. Chem. Soc. **116**, 11436–11443 (1994)
69. S. Suzuki, P.G. Green, R.E. Bumgarner, S. Dasgupta, W.A. Goddard, G.A. Blake, Science **257**, 942–944 (1992)
70. W.C. Wiley, I.H. McLaren, Rev. Sci. Instrum. **26**, 1150 (1955)
71. T. Schindler, C. Berg, G. Niedner-Schatteburg, V.E. Bondybey, Chem. Phys. Lett. **250**, 301–308 (1996)
72. S. Sato, N. Mikami, J. Phys. Chem. **100**, 4765–4769 (1996)
73. T. Sawamura, A. Fujii, S. Sato, T. Ebata, N. Mikami, J. Phys. Chem. **100**, 8131–8138 (1996)
74. K. Kleinermanns, C. Janzen, D. Spangenberg, M. Gerhards, J. Phys. Chem. A **103**, 5232–5239 (1999)
75. Z. Shi, J.V. Ford, S. Wei, J.A.W. Castleman, J. Chem. Phys. **99**, 8009–8015 (1993)

76. H.C. Chang, C.C. Wu, J.L. Kuo, Int. Rev. Phys. Chem. **24**, 553–578 (2005)
77. J.-L. Kuo, M.L. Klein, J. Chem. Phys. **122**, 024516 (2005)
78. M.P. Hodges, D.J. Wales, Chem. Phys. Lett. **324**, 279–288 (2000)
79. A.D. Becke, J. Chem. Phys. **98**, 5648–5652 (1993)
80. C. Lee, W. Yang, R.G. Parr, Phys. Rev. B **37**, 785 (1988)
81. V. Buch, Data bank on ice and icy particles, http://www.fh.huji.ac.il/∼viki/databank/IceParticles.html
82. D.J. Wales, J.P.K. Doye, A. Dullweber, M.P. Hodges, F.Y. Naumkin, F. Calvo, J. Hernández-Rojas, T.F. Middleton, http://www-wales.ch.cam.ac.uk/CCD.html
83. Y. Maréchal, *The Hydrogen Bond and the Water Molecule* (Elsevier, Amsterdam, 2007)
84. M.J. Frisch, G.W. Trucks, H.B. Schlegel, G.E. Scuseria, M.A. Robb, J.R. Cheeseman, J.A. Montgomery Jr, T. Vreven, K.N. Kudin, J.C. Burant, J.M. Millam, S.S. Iyengar, J. Tomasi, V. Barone, B. Mennucci, M. Cossi, G. Scalmani, N. Rega, G.A. Petersson, H. Nakatsuji, M. Hada, M. Ehara, K. Toyota, R. Fukuda, J. Hasegawa, M. Ishida, T. Nakajima, Y. Honda, O. Kitao, H. Nakai, M. Klene, X. Li, J.E. Knox, H.P. Hratchian, J.B. Cross, V. Bakken, C. Adamo, J. Jaramillo, R. Gomperts, R.E. Stratmann, O. Yazyev, A.J. Austin, R. Cammi, C. Pomelli, J.W. Ochterski, P.Y. Ayala, K. Morokuma, G.A. Voth, P. Salvador, J.J. Dannenberg, V.G. Zakrzewski, S. Dapprich, A.D. Daniels, M.C. Strain, O. Farkas, D.K. Malick, A.D. Rabuck, K. Raghavachari, J.B. Foresman, J.V. Ortiz, Q. Cui, A.G. Baboul, S. Clifford, J. Cioslowski, B.B. Stefanov, G. Liu, A. Liashenko, P. Piskorz, I. Komaromi, R.L. Martin, D.J. Fox, T. Keith, M.A. Al-Laham, C.Y. Peng, A. Nanayakkara, M. Challacombe, P.M.W. Gill, B. Johnson, W. Chen, M.W. Wong, C. Gonzalez, J.A. Pople, Gaussian 03, Revision E.01 (Gaussian, Inc., Wallingford CT, 2004)
85. M.J. Frisch, G.W. Trucks, H.B. Schlegel, G.E. Scuseria, M.A. Robb, J.R. Cheeseman, G. Scalmani, V. Barone, B. Mennucci, G.A. Petersson, H. Nakatsuji, M. Caricato, X. Li, H.P. Hratchian, A.F. Izmaylov, J. Bloino, G. Zheng, J.L. Sonnenberg, M. Hada, M. Ehara, K. Toyota, R. Fukuda, J. Hasegawa, M. Ishida, T. Nakajima, Y. Honda, O. Kitao, H. Nakai, T. Vreven, J.A. Montgomery Jr., J. E. Peralta, F. Ogliaro, M. Bearpark, J.J. Heyd, E. Brothers, K.N. Kudin, V.N. Staroverov, R. Kobayashi, J. Normand, K. Raghavachari, A. Rendell, J.C. Burant, S.S. Iyengar, J. Tomasi, M. Cossi, N. Rega, N.J. Millam, M. Klene, J.E. Knox, J.B. Cross, V. Bakken, C. Adamo, J. Jaramillo, R. Gomperts, R.E. Stratmann, O. Yazyev, A.J. Austin, R. Cammi, C. Pomelli, J.W. Ochterski, R.L. Martin, K. Morokuma, V.G. Zakrzewski, G.A. Voth, P. Salvador, J.J. Dannenberg, S. Dapprich, A.D. Daniels, O. Farkas, J.B. Foresman, J.V. Ortiz, J. Cioslowski, D.J. Fox, Gaussian 09, Revision B.01 (Gaussian, Inc., Wallingford CT, 2009)
86. P. Flukiger, H.P. Luthi, S. Portmann, J. Weber, MOLEKEL 4.3, Swiss Center for Scientific Computing, Manno, Switzerland, 2000–2002
87. T. Miyake, M. Aida, Chem. Phys. Lett. **363**, 106–110 (2002)
88. S. Maeda, K. Ohno, J. Phys. Chem. A **111**, 4527–4534 (2007)
89. K. Mizuse, N. Mikami, A. Fujii, Angew. Chem. Int. Ed. **49**, 10119–10122 (2010)
90. Y. Matsuda, M. Mori, M. Hachiya, A. Fujii, N. Mikami, J. Chem. Phys. **125**, 164320 (2006)
91. S. Enomoto, M. Miyazaki, A. Fujii, N. Mikami, J. Phys. Chem. A **109**, 9471–9480 (2005)
92. Y.S. Wang, J.C. Jiang, C.L. Cheng, S.H. Lin, Y.T. Lee, H.C. Chang, J. Chem. Phys. **107**, 9695–9698 (1997)
93. J.C. Jiang, Y.S. Wang, H.C. Chang, S.H. Lin, Y.T. Lee, G. Niedner-Schatteburg, J. Am. Chem. Soc. **122**, 1398–1410 (2000)
94. J.C. Jiang, J.C. Chang, B.C. Wang, S.H. Lin, Y.T. Lee, H.C. Chang, Chem. Phys. Lett. **289**, 373–382 (1998)
95. K. Suhara, A. Fujii, K. Mizuse, N. Mikami, J.L. Kuo, J. Chem. Phys. **126**, 194306 (2007)
96. C.K. Lin, C.C. Wu, Y.S. Wang, Y.T. Lee, H.C. Chang, J.L. Kuo, M.L. Klein, Phys. Chem. Chem. Phys. **7**, 938–944 (2005)
97. J.-D. Chai, M. Head-Gordon, Phys. Chem. Chem. Phys. **10**, 6615–6620 (2008)
98. Y. Zhao, D. Truhlar, Theor. Chem. Acc. **120**, 215–241 (2008)
99. Y. Zhao, D.G. Truhlar, Acc. Chem. Res. **41**, 157–167 (2008)

100. K.E. Riley, M. Pitonak, P. Jurecka, P. Hobza, Chem. Rev. **110**, 5023–5063 (2010)
101. C.J. Burnham, S.S. Xantheas, J. Chem. Phys. **116**, 5115 (2002)
102. G.S. Fanourgakis, S.S. Xantheas, J. Phys. Chem. A **110**, 4100–4106 (2006)
103. A.A. El-Azhary, H.U. Suter, J. Phys. Chem. **100**, 15056–15063 (1996)
104. K. Ohno, M. Okimura, N. Akai, Y. Katsumoto, Phys. Chem. Chem. Phys. **7**, 3005–3014 (2005)
105. P. Hobza, J. Sponer, T. Reschel, J. Comput. Chem. **16**, 1315–1325 (1995)
106. S.S. Xantheas, E. Apra, J. Chem. Phys. **120**, 823–828 (2004)
107. A.Y. Zasetsky, A.F. Khalizov, M.E. Earle, J.J. Sloan, J. Phys. Chem. A **109**, 2760–2764 (2005)
108. M.S. Bergren, D. Schuh, M.G. Sceats, S.A. Rice, J. Chem. Phys. **69**, 3477 (1978)
109. J.P. Devlin, C. Joyce, V. Buch, J. Phys. Chem. A **104**, 1974–1977 (2000)

http://www.springer.com/978-4-431-54311-4

Spectroscopic Investigations of Hydrogen Bond Network Structures in Water Clusters

Mizuse, K.

2013, XIII, 175 p., Hardcover
ISBN: 978-4-431-54311-4